

EVOLUTION OF MASSIVE PROTOSTARS WITH HIGH ACCRETION RATES

TAKASHI HOSOKAWA AND KAZUYUKI OMUKAI

Division of Theoretical Astronomy, National Astronomical Observatory of Japan, Mitaka, Tokyo 181-8588,
Japan

hosokawa@th.nao.ac.jp; omukai@th.nao.ac.jp

Draft version September 3, 2018

ABSTRACT

Formation of massive stars by accretion requires a high accretion rate of $\dot{M}_* > 10^{-4} M_\odot/\text{yr}$ to overcome the radiation pressure barrier of the forming stars. Here, we study evolution of protostars accreting at such high rates, by solving the structure of the central star and the inner accreting envelope simultaneously. The protostellar evolution is followed starting from small initial cores until their arrival at the stage of the Zero-Age Main Sequence (ZAMS) stars. An emphasis is put on evolutionary features different from those with a low accretion rate of $\dot{M}_* \sim 10^{-5} M_\odot/\text{yr}$, which is presumed in the standard scenario for low-mass star formation. With the high accretion rate of $\dot{M}_* \sim 10^{-3} M_\odot/\text{yr}$, the protostellar radius becomes very large and exceeds $100 R_\odot$. Unlike the cases of low accretion rates, deuterium burning hardly affects the evolution, and the protostar remains radiative even after its ignition. It is not until the stellar mass reaches $\simeq 40 M_\odot$ that hydrogen burning begins and the protostar reaches the ZAMS phase, and this ZAMS arrival mass increases with the accretion rate. These features are similar to those of the first star formation in the universe, where high accretion rates are also expected, rather than to the present-day low-mass star formation. At a very high accretion rate of $> 3 \times 10^{-3} M_\odot/\text{yr}$, the total luminosity of the protostar becomes so high that the resultant radiation pressure inhibits the growth of the protostars under steady accretion before reaching the ZAMS stage. Therefore, the evolution under the critical accretion rate $3 \times 10^{-3} M_\odot/\text{yr}$ gives the upper mass limit of possible pre-main-sequence stars at $\simeq 60 M_\odot$. The upper mass limit of MS stars is also set by the radiation pressure onto the dusty envelope under the same accretion rate at $\simeq 250 M_\odot$. We also propose that the central source enshrouded in the Orion KL/BN nebula has effective temperature and luminosity consistent with our model, and is a possible candidate for such protostars growing under the high accretion rate.

Subject headings: accretion – stars: early-type – stars: evolution – stars: formation – stars: pre-main-sequence

1. INTRODUCTION

Massive ($> 8 M_\odot$) stars make significant impacts on the interstellar medium via various feedback processes; e.g., UV radiation, stellar winds, and supernova explosions. Such feedback processes sometimes trigger or regulate nearby star-formation activity. Their thermal and kinetic effects are important factors in the phase cycle of the interstellar medium. Strong coherent feedback by many massive stars causes galactic-scale dynamical phenomena, such as galactic winds. Furthermore, massive stars dominate the light from distant galaxies. The cosmic star formation rate is mostly estimated with the light observed from massive stars (e.g., Madau et al. 1996; Hopkins & Beacom 2006). Despite such importance, the question of the formation process of massive stars still remains open. As for lower-mass stars, there is a widely-accepted formation scenario, where gravitational collapse of molecular cloud cores leads to subsequent mass accretion onto tiny protostars (e.g., Shu, Adams & Lizano 1987). If one directly applies this scenario to massive star formation, however, some difficulties arise in the main accretion phase (e.g., see Zinnecker & Yorke 2007; McKee & Ostriker 2007, for recent reviews). The main difficulty in the formation of massive stars is the very strong radiation pressure acting on a dusty envelope. The radiative repulsive effect becomes quite strong at the dust destruction front, where the accretion flow gets much of the outward momentum of radiation. Therefore, a necessary condition for massive star formation is to overcome this barrier at the dust destruction front. However, some theoretical work has shown that the accretion rate of $\dot{M}_* \sim 10^{-5} M_\odot/\text{yr}$ expected of lower-mass protostars is too low to overcome the barrier (e.g., Wolfire & Cassinelli 1987, hereafter WC87). Because of this difficulty, various scenarios different from the standard accretion paradigm have been proposed such as stellar mergers (e.g., Stahler, Palla & Ho 2000) and competitive accretion (e.g., Bonnell, Bate & Zinnecker 1998).

An origin of this disputed situation is uncertainty concerning the initial condition for massive star formation. This uncertainty partly originates from the scarcity of massive stars; most of the massive star forming regions are distant. In addition, the initial condition is easily disrupted by feedback from newly formed massive stars. Since the accretion rate reflects the thermal state of the original molecular core, it is still uncertain which rates should be favored for growing high-mass protostars. In fact, some observations of young high-mass sources suggest high accretion rates. Signatures of infall motion are detected with various line observations toward high-mass protostellar objects (HMPOs) and hyper-/ultra-compact H II regions, and the derived accretion rates are $10^{-4} - 10^{-3} M_\odot/\text{yr}$ (e.g., Fuller, Williams & Sridharan 2005; Beltrán et al. 2006; Keto & Wood 2006). Similar high accretion rates are also inferred by SED fitting of hot cores (Osorio, Lizano & D'Alessio 1999) and HMPOs (Fazal et al. 2007; Kumar & Grave 2008). Molecular outflows are also ubiquitous in high-mass star-forming regions, and estimated high mass outflow rates also suggest high accretion rates

(e.g., Beuther et al. 2002; Zhang et al. 2005). Such high accretion rates have the advantage of overcoming the radiation pressure barrier (Larson & Starrfield 1971; Kahn 1974). Theoretically, Nakano et al. (2000) have suggested a protostar growing at the very high accretion rate of $\sim 10^{-2} M_{\odot}/\text{yr}$ to explain the low radiation temperature of scattered light from Orion KL region (Morino et al. 1998). McKee & Tan (2002, 2003) have predicted that massive molecular cloud cores, from which a few massive stars form, should be dominated by supersonic turbulence, envisioning that such cores, if they exist, are embedded in a high-pressure environment. Krumholz, Klein & McKee (2007) have simulated collapse of the turbulent cores performing radiation-hydrodynamical calculations, and demonstrated that the accretion rates attain more than $10^{-4} M_{\odot}/\text{yr}$ in their simulations. Some recent observations are getting a close look at the initial condition of massive star formation, and have found strong candidates for high-mass pre-stellar cores (e.g., Rathborne, Simon & Jackson 2007; Motte et al. 2007). Further detailed observations will verify the scenario.

The main targets of this paper are protostars growing at the high accretion rates of $\dot{M}_{*} \geq 10^{-4} M_{\odot}/\text{yr}$. Detailed modeling of such protostars should be useful for future high-resolution observations and simulations of massive star formation. However, previous studies on such protostars are fairly limited. The protostellar evolution has been well studied for low-mass ($< 1 M_{\odot}$) and intermediate-mass ($< 8 M_{\odot}$) protostars by detailed numerical calculations solving the stellar structure, but these studies have focused on evolution at the low accretion rate of $\sim 10^{-5} M_{\odot}/\text{yr}$ (e.g., Stahler, Shu & Taam 1980a,b, hereafter SST80a,b; Palla & Stahler 1990, 1991, hereafter PS91, 1992; Beech & Mitalas 1994) Maeder and coworkers have calculated the protostellar evolution under accretion rates growing with the stellar mass, which finally exceeds $10^{-4} M_{\odot}/\text{yr}$ (Bernasconi & Maeder 1996; Behrend & Maeder 2001; Norberg & Maeder 2000), but it is still uncertain how the evolution changes with accretion rates, and which physical mechanisms cause differences. Some authors have used polytropic one-zone models originally invented for low accretion rates even at such a high rate (e.g., Nakano et al. 2000; McKee & Tan 2003; Krumholz & Thompson 2007), but its validity remains obscure owing to the lack of detailed calculations. By coincidence, the similar high accretion rates are expected for protostars forming in the early universe (e.g., Omukai & Nishi 1998; Yoshida et al. 2006). This simply reflects high temperatures in primordial pre-stellar clouds. Evolution of such primordial protostars has been studied by Stahler, Palla & Salpeter (1986, hereafter SPS86) and Omukai & Palla (2001, 2003). Therefore, our other motivation is to investigate how the protostellar evolution changes with metallicities.

To summarize, our goal in this paper is to answer the following questions;

- What are the properties of massive protostars (e.g., radius, luminosity, and effective temperature) growing at high accretion rates? Can we observe any signatures of their characteristic properties?
- How different are high-mass protostars from low- and intermediate-mass ones, for which lower accretion rates are presumed? How about the difference from the protostellar evolution of primordial stars? Furthermore, if the protostellar evolution significantly varies with accretion rates and metallicities, what causes such differences?
- What are the consequences of protostellar evolution with high accretion rates for the formation and feedback processes of massive stars? How massive can a star get before its arrival at the Zero-Age Main Sequence (ZAMS)? What is the maximum mass of stars that can be formed?

In order to answer these questions, we solve the structure of accreting protostars with various accretion rates and metallicities with detailed numerical calculations (also see Yorke & Bodenheimer 2008, for a similar effort).

The organization of this paper is as follows: In § 2, we briefly review the basic procedure to construct numerical models of accreting protostars and their surrounding envelopes. The subsequent § 3 is the main part of this paper, where our numerical results are presented. First, we investigate the protostellar evolution of two fiducial cases with the accretion rates of 10^{-3} and $10^{-5} M_{\odot}/\text{yr}$ in § 3.1 and § 3.2. After that, we show more general variations of protostellar evolution, e.g., mass accretion rates in § 3.3, and metallicities in § 3.4. In § 3.5, we present the protostellar evolution at very high accretion rates exceeding $10^{-3} M_{\odot}/\text{yr}$, and show that the steady accretion is limited by a radiation pressure barrier acting on a gas envelope. We further discuss some implications based on our numerical results. In § 4, we examine which feedback effects can affect the growth of protostars for a given accretion rate. We also explore some observational possibilities of detecting signatures of the supposed high accretion rates in § 5. Finally, § 6 is assigned to summary and conclusions.

2. NUMERICAL MODELING

2.1. Outline

We employ the method of calculation developed by SPS86 and PS91. In this section, only the outline of modeling is overviewed. A detailed description of the method is presented in Appendix A.

As shown in Figure 1, the whole system can be divided into two parts of different nature, i.e., an accreting envelope and a hydrostatic core. This hydrostatic core is also called a protostar since it eventually grows into a star by accretion. The outer part of the accreting envelope contains dust grains, while the warm ($\gtrsim 2000\text{K}$) part near the protostar is dust-free as a result of their evaporation. Despite the absence of the dust, the innermost dense part of the envelope becomes optically thick to gas continuum opacity and the photosphere appears outside the accretion shock front in the case of a high accretion rate. Such an inner envelope is called the radiative precursor. We here consider only the protostar and the radiative precursor under a given constant accretion rate (see Fig. 1). The dusty outer envelope is not included in our formulation, although stellar feedback exerted on the envelope may be important in the last stage of accretion: the

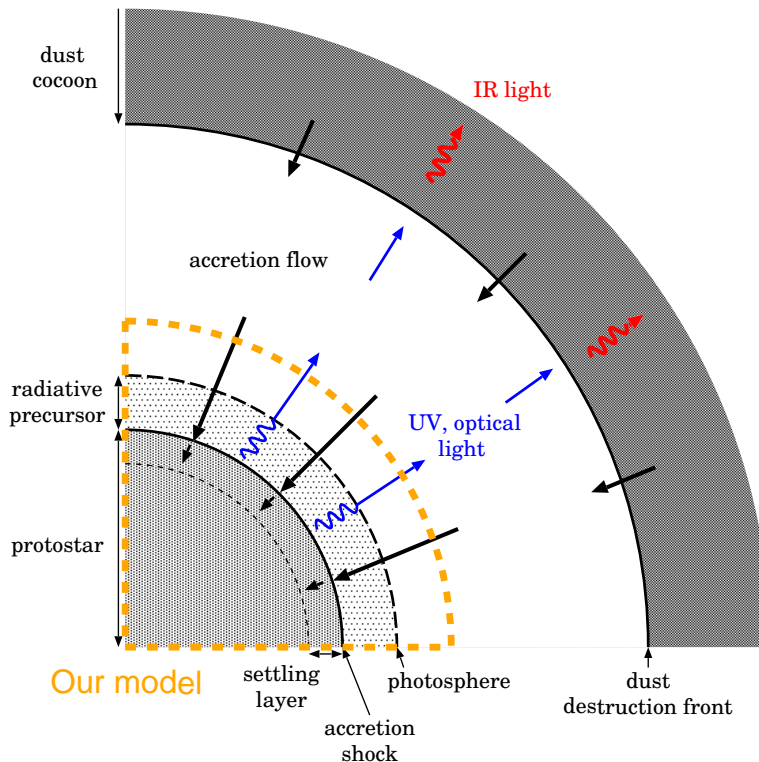


FIG. 1.— A schematic figure of a protostar and surrounding accretion flow. The accretion shock forms at the stellar surface. When the flow becomes optically thick before hitting on the shock, the photosphere forms outside the stellar surface. The optically thick part of the accreting envelope is called the radiative precursor. A dust cocoon surrounds the protostar at larger radius. The inner boundary of the dust cocoon is a dust destruction front. Most of the light from the protostar is absorbed at the dust destruction front once, and reemitted as infrared light. In our calculations, we solve the detailed structure only of the protostar and accretion flow far inside the dust destruction front, which are enclosed by the thick dashed line. We discuss possible feedback effects on the outer dust cocoon in § 4.

mass accretion can be terminated finally by radiation pressure or other protostellar feedback processes (e.g., stellar wind) exerted on the dusty envelope. For the present, we presume that the protostar continues to grow at a given mass accretion rate and look for solutions of protostars with steady-state accretion. Discussion on feedback that halts the accretion is deferred to § 4.

We calculate protostellar evolution by constructing a time sequence of quasi-steady structures of the protostar and accreting envelope. We solve the stellar structure equations for the protostar. For the accreting envelope, we adopt different treatments depending on whether or not it is opaque to the gas opacity. If the flow remains optically thin and no radiative precursor exists, the free-fall is assumed to be outside the star. For the opaque flow, on the other hand, we solve the structure of the radiative precursor by using the equations for a steady-state flow. At the outer boundary, which is taken to be at the photosphere, the flow is assumed to be in free fall. After solving the protostar and accreting envelope individually, these solutions are connected at the accretion shock front by the radiative shock condition (e.g., SST80a). The shooting method is adopted for solving radial structure. This procedure is repeated until the required boundary conditions are satisfied.

We start calculation from a very small protostar, typically $M_{*,0} = 0.01M_{\odot}$. The initial models are constructed following SST80b (see Appendix A.2 for detail). Although this choice is rather arbitrary, the star converges immediately to a certain structure appropriate for accretion at a given rate. Specific conditions of the initial models do not affect the evolution thereafter. The evolution is followed by increasing the stellar mass owing to accretion step by step. This procedure is repeated until the star reaches the ZAMS phase after the onset of hydrogen burning. In a few runs with very high accretion rates, however, steady accretion becomes impossible before arrival at the ZAMS and the calculation is terminated at this moment.

2.2. Calculated Runs

The calculated runs and their input parameters are listed in Table.1. Cases with a wide range of accretion rates are studied, starting from $10^{-6} M_{\odot}/\text{yr}$ up to $6 \times 10^{-3} M_{\odot}/\text{yr}$. The lowest values of $10^{-6} - 10^{-5} M_{\odot}/\text{yr}$ are typical for low-mass star formation, while high rates $> 10^{-4} M_{\odot}/\text{yr}$ are those envisaged in the accretion scenario of massive star formation. The initial deuterium abundance of $[D/H] = 2.5 \times 10^{-5}$ is adopted as a fiducial value, following previous work (e.g., SST80a, PS91) for comparison. To assess the role of deuterium burning, we also calculate “noD” runs, where the deuterium is absent. Most of the runs are for the solar metallicity $Z_{\odot} (=0.02)$. Two runs with 10^{-3} and $10^{-5} M_{\odot}/\text{yr}$ are

Table 1. Calculated Runs and Input Parameters

Run	\dot{M}_* (M_\odot/yr) ^a	[D/H] (10^{-5}) ^b	Z^c	$M_{*,0}$ (M_\odot) ^d	$R_{*,0}$ (R_\odot) ^e	reference ^f
MD6x3	6×10^{-3}	2.5	0.02	0.5	43.9	§ 3.5
MD4x3	4×10^{-3}	2.5	0.02	0.3	33.0	§ 3.5
MD3x3	3×10^{-3}	2.5	0.02	0.2	27.8	§ 3.5
MD3x3-z0	3×10^{-3}	2.5	0.0	0.2	26.4	§ 3.5
MD3	10^{-3}	2.5	0.02	0.05	15.5	§ 3.1, 3.3, 3.4, 3.5
MD3-noD	10^{-3}	0.0	0.02	0.05	15.5	§ 3.3
MD3-z0	10^{-3}	2.5	0.0	0.05	13.0	§ 3.4
MD4	10^{-4}	2.5	0.02	0.01	7.9	§ 3.3
MD4-noD	10^{-4}	0.0	0.02	0.01	7.9	§ 3.3
MD5	10^{-5}	2.5	0.02	0.01	3.7	§ 3.2, 3.3, 3.4
MD5-noD	10^{-5}	0.0	0.02	0.01	3.7	§ 3.2, 3.3
MD5-dh1	10^{-5}	1.0	0.02	0.01	3.7	Appendix B.1
MD5-dh3	10^{-5}	3.0	0.02	0.01	3.7	Appendix B.1
MD5-z0	10^{-5}	2.5	0.0	0.01	2.9	§ 3.4
MD5-ps91 ^g	10^{-5}	2.5	0.02	1.0	4.2	Appendix B.2
MD6	10^{-6}	2.5	0.02	0.01	1.6	§ 3.3
MD6-noD	10^{-6}	0.0	0.02	0.01	1.6	§ 3.3

a : mass accretion rate, b : initial number fractional abundance of deuterium, c : metallicity, d : mass of initial core model, e : radius of initial core model, f : subsections where numerical results of each run are presented, g : initial model is the same as PS91

calculated for the metal-free gas (runs MD3-z0 and MD5-z0) to see the effects of different metallicities. For $10^{-5} M_\odot/\text{yr}$, variations in deuterium abundances (runs MD5-dh1 and MD5-dh3) and in initial models (MD5-ps91) are studied and presented in Appendix B for comparison with previous calculations.

Initial stellar mass in each run is taken to be sufficiently small, typically $M_{*,0} = 0.01 M_\odot$. For high accretion rates $\dot{M}_* \geq 10^{-3} M_\odot/\text{yr}$, somewhat more massive initial stars (see Table.1) are used since convergence of calculation was not achieved for lower mass ones. The radii of initial models are also listed in Table.1.

3. PROTOSTELLAR EVOLUTION WITH DIFFERENT ACCRETION RATES

There are two important timescales for evolution of accreting protostars. The first one is the accretion timescale,

$$t_{\text{acc}} \equiv \frac{M_*}{\dot{M}_*}, \quad (1)$$

over which the protostar grows by mass accretion. This is an evolutionary timescale of our calculations. The second one is the Kelvin-Helmholtz (KH) timescale,

$$t_{\text{KH}} \equiv \frac{GM_*^2}{R_*L_*}, \quad (2)$$

over which the protostar loses energy by radiation. The balance among these timescales is crucial to the protostellar evolution. When $t_{\text{KH}} > t_{\text{acc}}$, the radiative energy loss hardly affects the protostellar evolution. The evolution is controlled only by the effect of mass accretion. When $t_{\text{KH}} < t_{\text{acc}}$, on the other hand, the evolution is mainly controlled by the radiative energy loss.

Luminosity from accreting protostars has two sources: one is from the stellar interior, the other from the accretion shock front. In this paper, we call the former the interior luminosity L_* , and the latter the accretion luminosity,

$$L_{\text{acc}} \equiv \frac{GM_*\dot{M}_*}{R_*}. \quad (3)$$

Total luminosity from the star is the sum of the interior and accretion luminosity: $L_{\text{tot}} = L_* + L_{\text{acc}}$. Note that the balance between t_{KH} and t_{acc} also determines the dominant component of luminosity from accreting protostars, i.e., the ratio L_{acc}/L_* is equivalent to $t_{\text{KH}}/t_{\text{acc}}$.

During the growth of the protostar, the KH timescale significantly decreases. As a result, the ratio $t_{\text{KH}}/t_{\text{acc}}$, which is initially very large, falls below unity in the protostellar evolution. Below, we show that the decrease of $t_{\text{KH}}/t_{\text{acc}}$ indeed leads to a variety of evolutionary phases of accreting protostars.

3.1. Case with High Accretion Rate $\dot{M}_* = 10^{-3} M_\odot/\text{yr}$

First, we see a protostar growing at a high accretion rate $\dot{M}_* = 10^{-3} M_\odot/\text{yr}$ (run MD3), which is relevant to massive star formation. The upper panel of Figure 2 shows evolution of the protostellar radius (thick solid) and the interior

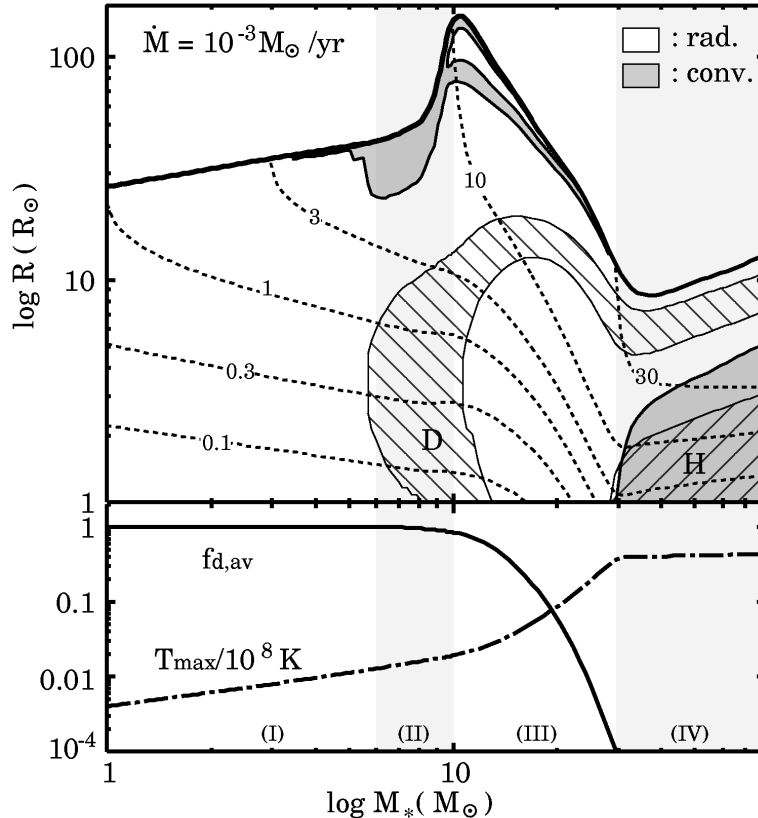


FIG. 2.— Evolution of a protostar with the accretion rate $\dot{M}_* = 10^{-3} M_\odot/\text{yr}$ (run MD3). *Upper panel*: The interior structure of the protostar. The thick solid curve represents the protostellar radius (R_*), which is the position of the accretion shock front. Convective layers are shown by gray-shaded area. The hatched areas indicate layers of active nuclear burning, where the energy production rate exceeds the steady rate $L_{D,st}/M_*$ for the deuterium burning, and L_*/M_* for the hydrogen burning. The thin dotted curves represent the loci of mass coordinates; $M = 0.1, 0.3, 1, 3, 10,$ and $30 M_\odot$. *Lower panel*: Evolution of the mass-averaged deuterium concentration, $f_{d,av}$ (solid line) and the maximum temperature within the star T_{\max} (dot-dashed line). In both panels, the shaded background shows the four evolutionary phases; (I) adiabatic accretion, (II) swelling, (III) Kelvin-Helmholtz contraction, and (IV) main-sequence accretion phases.

structure as a function of the protostellar mass. The mass increases monotonically with time t , $M_* = M_{*,0} + \dot{M}_* t$, and can be regarded as a time coordinate. The entire evolution can be divided into the following four phases according to their characteristic features; (I) the adiabatic accretion (for $M_* \lesssim 6 M_\odot$), (II) swelling ($6 M_\odot \lesssim M_* \lesssim 10 M_\odot$), (III) KH contraction ($10 M_\odot \lesssim M_* \lesssim 30 M_\odot$), and (IV) main-sequence accretion ($M_* \gtrsim 30 M_\odot$) phases. Below, we see the protostellar evolution in each phase.

Adiabatic Accretion Phase Upper panels of Figure 3 present the evolution of entropy profile within the protostar. This shows that the entropy profiles at different epochs completely overlap: at a fixed mass element, the specific entropy remains constant. The entropy is originally generated at the accretion shock front, and embedded into the stellar interior. Thus, during this earliest phase, the entropy profile inside the star just traces the history of entropy at the post-shock point. Owing to a high value of opacity, radiative heat transport is inefficient in the interior of the protostar. This makes the interior luminosity small, then $t_{\text{KH}} \gg t_{\text{acc}}$ in this phase (see Fig. 5 bottom panel, below). Once the accreted matter settles into the opaque interior, the specific entropy is just conserved.

The snapshots of the luminosity profile are also presented in lower panels of Figure 3. Near the surface is a spiky structure where the gradient $\partial L/\partial M$ is very large owing to a sharp decrease in opacity there. Although a significant entropy loss occurs in this luminosity spike as indicated by the relation $(\partial s/\partial t)_M \simeq -1/T (\partial L/\partial M)_t$ (from eq. (A3)), this layer is extremely thin and the time for a mass element to pass through it is so short that the entropy hardly changes. This can be confirmed by comparing the two timescales; the local accretion time

$$t_{\text{acc},s}(m) = \frac{m}{\dot{M}_*}, \quad (4)$$

and local cooling time

$$t_{\text{cool},s}(m) = \frac{m \delta s}{\int_0^m \frac{1}{T} \frac{\partial L}{\partial m} dm'}, \quad (5)$$

where $m = M_* - M$ is the depth (in mass coordinate) of a mass shell from the accretion shock, and δs denotes arbitrary

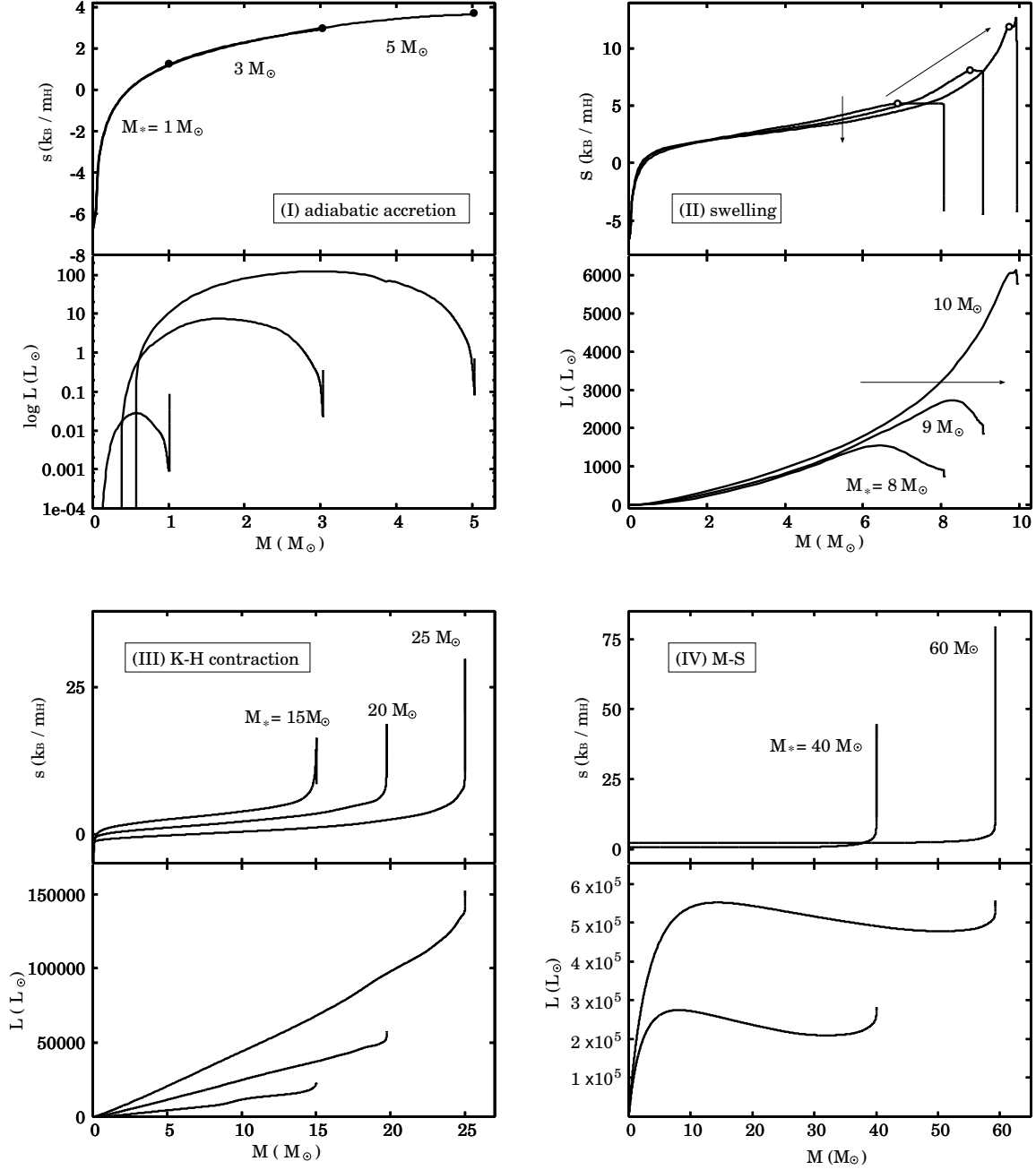


FIG. 3.— Radial profiles of the specific entropy and the luminosity at different epochs for the protostar with the accretion rate $\dot{M}_* = 10^{-3} M_\odot/\text{yr}$ (run MD3) shown as functions of the mass coordinate M . For each snapshot, total stellar mass (M_*) at its moment is labeled. The four panels correspond to the four evolutionary phases, (I) adiabatic accretion (upper left), (II) swelling (upper right), (III) Kelvin-Helmholtz contraction (lower left), and (IV) main-sequence accretion (lower right) phases. In the entropy profiles of the upper left panel, the filled circles denote the post-shock values. In the upper right panel, the open circles indicate the bottom edges of convective layers.

small entropy change. The former, $t_{\text{acc},s}$, is the time for a thin shell of mass m at the surface to be replaced by the newly accreted material, while the latter, $t_{\text{cool},s}$, is the time for the same shell to lose the entropy $m \delta s$ by outward radiation. Comparison between these timescales in the settling layer is presented in Figure 4, where $\delta s = 0.1 k_B/m_H$ is adopted for numerical evaluation. This indicates that $t_{\text{acc},s}$ is always shorter than $t_{\text{cool},s}$: the accreted material is swiftly embedded in the interior before losing the entropy δs by radiation. Therefore, the adiabaticity remains valid in spite of the spike in luminosity profile. Note that the short $t_{\text{acc},s}$ is a result of the high accretion rate. We will see that the situation changes for much lower accretion rates in § 3.2 and 3.3 below.

With increasing protostellar mass M_* , the accretion shock strengthens and the post-shock entropy increases. Then, the interior entropy increases as well. This causes a gradual expansion of the stellar radius in the adiabatic accretion phase

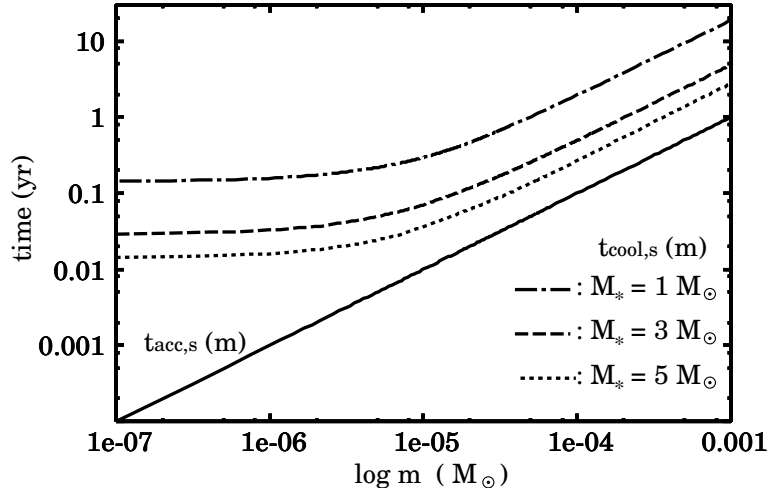


FIG. 4.— Comparison between the local accretion and cooling timescales in the surface settling layer, defined by equations (4) and (5). These timescales are shown as functions of the mass coordinate measured from the accretion shock front $m \equiv M_* - M$. The accretion timescale is presented by the solid line. The cooling timescales at $M_* = 1 M_\odot$, $3 M_\odot$, and $5 M_\odot$ are presented by the dot-dashed, dashed, and dotted lines, respectively.

(Fig. 2, upper panel). Using the typical density and pressure within a star of mass M_* and radius R_* (e.g., Cox & Giuli 1968);

$$\rho \sim \frac{M_*}{R_*^3}, \quad P \sim G \frac{M_*^2}{R_*^4}. \quad (6)$$

and the expression for specific entropy of ideal monatomic gas

$$s = \frac{3\mathcal{R}}{2\mu} \ln \left(\frac{P}{\rho^{5/3}} \right) + const. \quad (7)$$

where \mathcal{R} is the gas constant and μ is the mean molecular weight, the stellar radius and entropy is related as (Stahler 1988);

$$R_* \propto M_*^{-1/3} \exp \left[\frac{2\mu}{3\mathcal{R}} s \right], \quad (8)$$

i.e., the stellar radius is larger for the higher entropy within the star. SPS86 have derived the mass-radius relation for protostars in the adiabatic accretion phase;

$$R_* \simeq 26 R_\odot \left(\frac{M_*}{M_\odot} \right)^{0.27} \left(\frac{\dot{M}_*}{10^{-3} M_\odot/\text{yr}} \right)^{0.41}, \quad (9)$$

under the condition that opacity in the radiative precursor is dominated by H^- bound-free absorption. As this condition holds in our case, our calculated mass-radius relation is in a good agreement with equation (9). Equation (9) suggests the large radius ($> 10 R_\odot$) of the rapidly-accreting protostar.

The interior of the protostar remains radiative throughout this phase (Fig. 2, upper panel): all the energy transport is via radiation. This is in high contrast with low \dot{M}_* ($\sim 10^{-5} M_\odot/\text{yr}$) cases, where most of the interior becomes convective owing to deuterium burning for $M_* \gtrsim 0.4 M_\odot$ (see Fig. 7 below). This can be attributed to a difference in the interior temperature. From equation (6), typical temperature within the star is

$$T = \frac{\mu}{\mathcal{R}} \frac{P}{\rho} \sim \frac{G}{\mathcal{R}} \frac{\mu M_*}{R_*}. \quad (10)$$

Therefore, the large stellar radius leads to the low temperature in the stellar interior. In fact, the maximum temperature in this phase does not exceed the threshold for deuterium burning (lower panel of Fig. 2).

Once the accreted matter has passed through the outermost layer with the luminosity spike, the luminosity gradient becomes much milder. The luminosity has a maximum at some radius: outside the luminosity maximum, the gradient $\partial L/\partial M < 0$, while $\partial L/\partial M > 0$ inside. This means that heat is removed from the deep interior and absorbed in the outer layer. This entropy transfer, however, remains small and does not modify the entropy distribution significantly during this phase. Efficiency of the outward entropy transfer is related to the value of opacity. In most of the stellar interior, major sources of opacity are bound-bound and bound-free transitions of heavy elements, which approximately obey Kramers' law, $\kappa \propto \rho T^{-3.5}$ (Hayashi, Hoshi & Sugimoto 1962; Clayton 1968). With the increase in stellar mass and then the interior

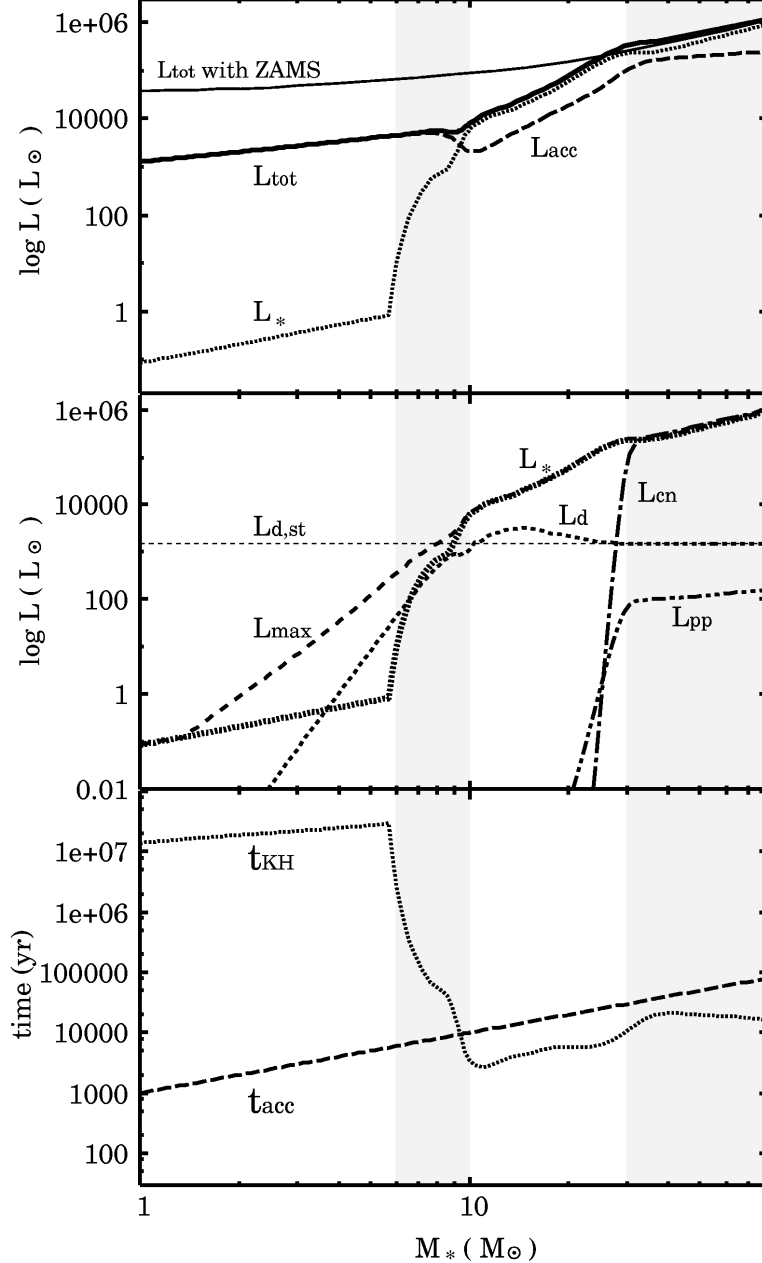


FIG. 5.— *Top panel*: Evolution of the interior luminosity L_* (dotted), accretion luminosity L_{acc} (dashed), and total luminosity $L_{\text{tot}} \equiv L_* + L_{\text{acc}}$ (solid) of an accreting protostar with $\dot{M}_* = 10^{-3} M_{\odot}/\text{yr}$ (run MD3). The total luminosity calculated with radius and luminosity of the ZAMS stars is also presented by the thin solid line. *Middle panel*: Evolution of various contributions to the interior luminosity of the protostar. The thick dotted line represents the stellar luminosity, L_* (also shown in the top panel). The total burning rate of each nuclear reaction is shown for the deuterium burning (L_{d} , coarse dotted), pp-chain (L_{pp} , dot-dot-dashed), and CN-cycle (L_{CN} , dot-dashed line). The horizontal coarse dotted line indicates the steady deuterium burning rate $L_{\text{d,st}}$. The maximum luminosity within the star is plotted with the coarse dashed line. *Bottom panel*: Evolution of the accretion timescale t_{acc} (dashed), and Kelvin-Helmholtz timescale t_{KH} (dotted) for the same protostar. In all panels, the shaded background shows the four evolutionary phases, as in Fig. 2.

temperature, the opacity decreases. This results in steady increase of the outward heat flux with evolution. In fact, as shown in the lower panels of Figure 3, the amplitude of the luminosity increases with the growth of the protostar. Also the maximum luminosity within the star L_{max} increases as a power-law function of M_* as seen in the middle panel of Figure 5. This dependence can be understood as follows: for a star with radiative stratification and Kramers' opacity, the luminosity scales as $L_{\text{rad}} \propto M_*^{11/2} R_*^{-1/2}$ (e.g., Cox & Giuli 1968). We have confirmed that L_{max} roughly obeys,

$$L_{\text{max}} \simeq 0.2 L_{\odot} \left(\frac{M_*}{M_{\odot}} \right)^{11/2} \left(\frac{R_*}{R_{\odot}} \right)^{-1/2} \quad (11)$$

in our calculations. Using equations (9) and (11), we obtain $L_{\max} \propto M_*^{5.4}$ for a constant accretion rate. When opacity becomes sufficiently small, the radiative heat transport becomes significant even in the deep interior. Consequently, the entropy distribution and thus stellar structure are drastically altered, which leads to the subsequent swelling phase.

Swelling Phase At the mass of about $6 M_\odot$, the protostar begins to swell up dramatically. The stellar radius suddenly increases by a factor of about three and eventually exceeds $100 R_\odot$. This swelling is caused by redistribution of entropy within the star. As explained above, the outward heat flow continues to increase, and ceases to be negligible. Figure 3 shows that the entropy distribution changes significantly with time, i.e., with M_* : the entropy decreases in the deep interior, and increases in the outer layer. The extent of the inner entropy-losing region becomes larger and larger, and approaches the surface, as more of the interior becomes less opaque.

As seen in the bottom panels of Figure 3, the peak of the luminosity, which is the boundary between the entropy-losing interior and the outer absorbing layer, gradually moves toward the surface with increasing height. This outward propagation of the luminosity peak is called the luminosity wave (SPS86). Only a thin outlying layer absorbs the entropy transported from the deep interior. This rapid increase of the entropy near the surface causes swelling of the radius. Actually, only a small fraction of mass near the surface contributes to this swelling. For example, at the maximum expansion of the radius $R_* \simeq 140 R_\odot$ at $M_* \simeq 10 M_\odot$, only 0.03% of the total mass is contained in the outer layers of $R_* > 70 R_\odot$.

Note that the swelling is not due to the shell burning of deuterium. Palla & Stahler (1990) have presented that a similar swelling occurring in intermediate-mass protostars at the low accretion rate of $\dot{M}_* = 10^{-5} M_\odot/\text{yr}$, and concluded that this is caused by the shell burning of deuterium. In our case, however, deuterium burning is not important for the swelling. Even in the run without deuterium burning (MD3-noD), the swelling is caused by redistribution of entropy in the same fashion (also see § 3.3 below). During this phase, the deuterium burning occurs in the inner region (Fig. 2, upper panel). Despite the active deuterium burning, most of the stellar interior remains radiative. Because of the higher entropy and thus lower density in the star, the opacity is lower in our case when the active deuterium burning begins. This allows efficient radiative transport of the generated entropy (Stahler 1988). The middle panel of Figure 5 shows that the maximum radiative luminosity L_{\max} always exceeds that by the deuterium burning L_D . This indicates a large capacity of radiative heat transport. Also a thin convective layer near the surface (Fig. 2) is not brought about by the deuterium burning. Although this layer receives the transported entropy from inside, the higher opacity due to ionization prevents the outward heat flow. This causes a negative entropy gradient and then convection near the surface.

Kelvin-Helmholtz Contraction With the approach of the luminosity wave to the surface, an increasing amount of energy flux escapes from the star without being absorbed inside. This results in a significant increase in the interior luminosity L_* for $M_* > 5M_\odot$ (Fig. 5) and thus the shorter KH timescale $t_{\text{KH}} (\propto 1/L_*)$ of the star. The arrival of the luminosity wave at the stellar surface marks the moment that all parts of the star begin to lose heat. Almost simultaneously, t_{KH} becomes as short as the accretion timescale t_{acc} (Fig. 5). While maintaining the virial equilibrium against the radiative energy loss, the protostar turns to contraction. This is the so-called KH contraction phase. The epoch of the radial turn-around is roughly estimated by equating t_{acc} and $t_{\text{KH},\text{lmax}} \equiv GM_*^2/R_*L_{\max}$, where L_{\max} is given by equation (11),

$$M_{*,\text{rmax}} = 10.8 M_\odot \left(\frac{\dot{M}_*}{10^{-3} M_\odot/\text{yr}} \right)^{2/9}. \quad (12)$$

In the above, we have omitted a weak dependence on R_* and just substituted $R_* \sim 10 R_\odot$ for simplicity. During the contraction of the protostar, the KH timescale remains slightly shorter than the accretion timescale. Since the ratio $t_{\text{KH}}/t_{\text{acc}}$, or equivalently L_*/L_{\max} , is less than unity, the interior luminosity exceeds the accretion luminosity and becomes the dominant source of the total luminosity of the protostar (upper panel of Fig. 5).

Since the stellar interior remains radiative in spite of the deuterium burning, the accreted deuterium is not transported to the deep interior by convection. Deuterium in the deep interior is thus soon consumed. Thereafter the deuterium burning continues in a shell-like outer layer (Fig. 2, upper panel). This surface burning proceeds at a rate slightly exceeding the steady-burning one (e.g., Palla & Stahler 1990),

$$L_{D,\text{st}} \equiv \dot{M}_* \delta_D = 1500 L_\odot \left(\frac{\dot{M}_*}{10^{-3} M_\odot/\text{yr}} \right) \left(\frac{[\text{D}/\text{H}]}{2.5 \times 10^{-5}} \right), \quad (13)$$

where δ_D is the energy available from the deuterium burning per unit gas mass. Consequently, the mass-averaged deuterium concentration $f_{\text{d,av}}$ significantly decreases during the KH contraction (Fig. 2, lower panel).

Arrival at a Main-sequence Star Phase With the KH contraction, the interior temperature increases gradually. At $M_* \simeq 20 M_\odot$ the maximum temperature reaches 10^7K and the nuclear fusion of hydrogen begins (Fig. 2). Although the hydrogen burning is initially dominated by the pp-chain reactions, energy generation by the CN-cycle reactions immediately overcome this. The energy production by the CN-cycle compensates radiative loss from the surface at $M_* \simeq 30 M_\odot$ (Fig. 5, middle), where the KH contraction terminates. A convective core emerges owing to the rapid

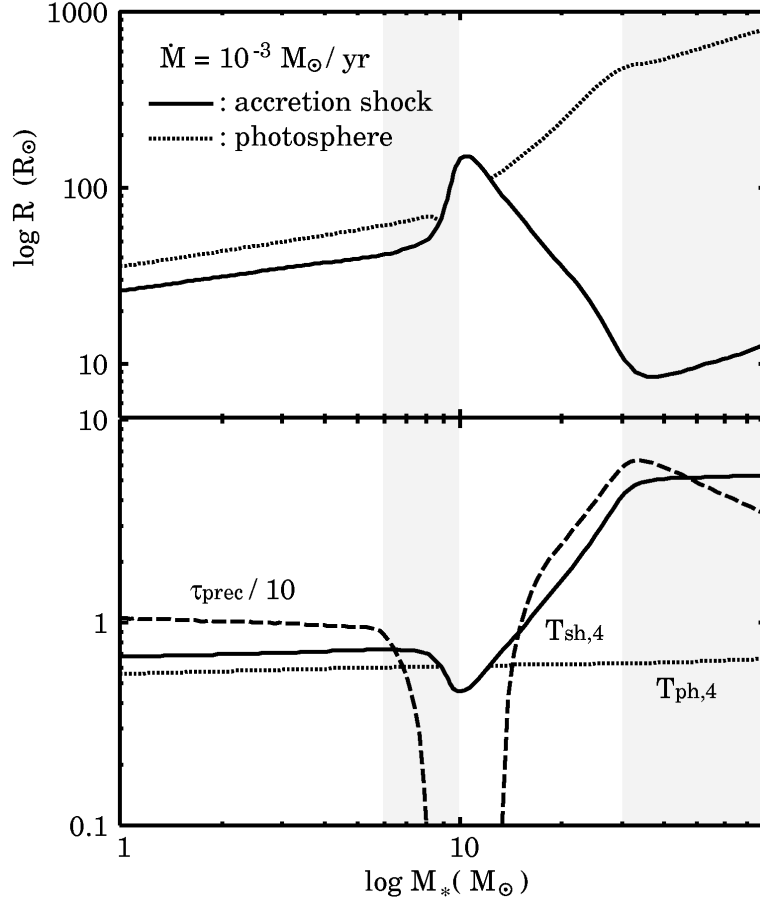


FIG. 6.— *Upper panel* : Positions of the accretion shock front (solid line), and photosphere (dotted line) of a growing protostar with $\dot{M}_* = 10^{-3} M_\odot/\text{yr}$ (run MD3). The layer between the accretion shock front and photosphere corresponds to the radiative precursor. *Lower panel* : the optical depth within the radiative precursor τ_{rec} , and effective temperatures at the photosphere T_{ph} and accretion shock front $T_{\text{sh}} \equiv (L_*/4\pi R_*^2 \sigma)^{1/4}$. The temperatures are normalized as $T_4 = (T/10^4\text{K})$. The shaded background shows the four evolutionary phases, as in Fig. 2.

entropy generation near the center. The stellar radius increase after that, obeying the mass-radius relation of main-sequence stars.

Evolution of the Radiative Precursor Figure 6 shows the evolution of protostellar (R_*) and photospheric (R_{ph}) radii. Except in a short duration, the photosphere is formed outside the stellar surface: the radiative precursor persists throughout most of the evolution. In the adiabatic accretion phase, the photospheric radius is slightly outside the protostellar radius and increases gradually with the relation $R_{\text{ph}} \simeq 1.4R_*$, which is derived analytically by SPS86. Although the precursor temporarily disappears in the swelling phase around $M_* \simeq 10M_\odot$, it emerges again in the subsequent KH contraction phase. In the KH contraction phase, the precursor extends spatially and becomes more optically thick. Due to the extreme temperature sensitivity of H^- bound-free absorption opacity, the region in the accreting envelope with temperature $\gtrsim 6000\text{K}$ becomes optically thick. Thus, the photospheric temperature T_{ph} remains at $6000 - 7000\text{K}$ throughout the evolution (Fig. 6, lower panel). Since the photospheric radius is related to the total luminosity by

$$R_{\text{ph}} = (L_{\text{tot}}/4\pi\sigma T_{\text{ph}}^4)^{1/2}, \quad (14)$$

for the constant T_{ph} , the rapid increase in the luminosity in the contraction phase causes the expansion of the photosphere.

3.2. Case with Low Accretion Rate $\dot{M}_* = 10^{-5} M_\odot/\text{yr}$

Next, we revisit the evolution of an accreting protostar under the lower accretion rate of $\dot{M}_* = 10^{-5} M_\odot/\text{yr}$ (run MD5). Although this case has been extensively studied by previous authors, a brief presentation should be helpful to underline the effects of different accretion rates on protostellar evolution. Different properties of the protostar even at the same

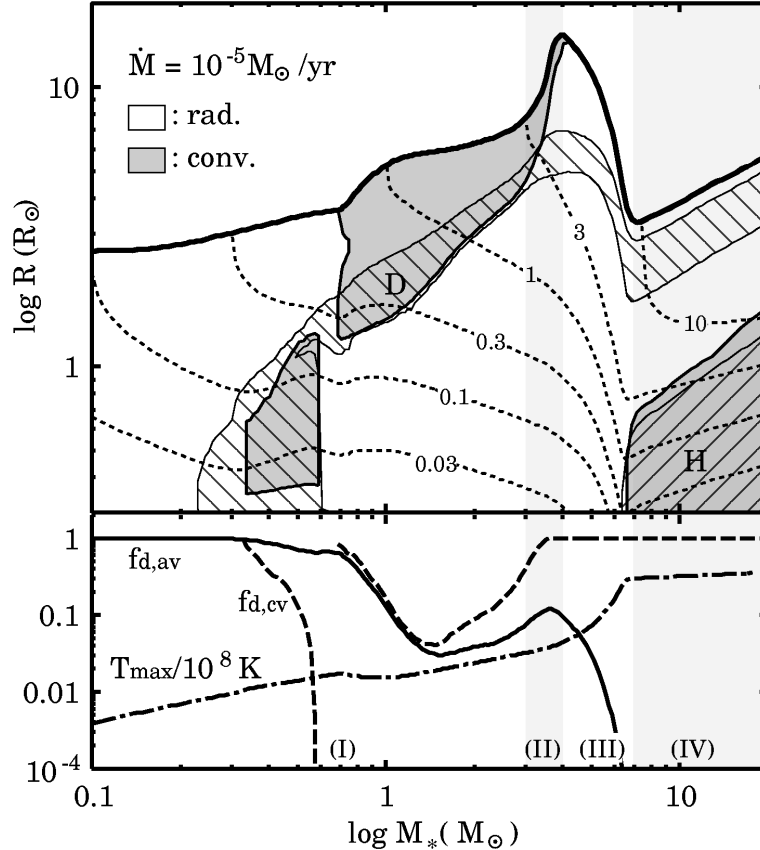


FIG. 7.— Same as Fig. 2 but for the lower accretion rate of $\dot{M}_* = 10^{-5} M_\odot/\text{yr}$ (run MD5). In the lower panel, deuterium concentration in the convective layer $f_{d,cv}$ is also presented. In both upper and lower panels, the shaded background shows the four evolutionary phases ; (I) convection, (II) swelling, (III) Kelvin-Helmholtz contraction, and (IV) main sequence accretion phases

accretion rate owing to updates from the previous works, e.g, initial models and opacity tables, will also be described. For a thorough comparison between our and some previous calculations, see appendix B.

The lower accretion rate means the longer accretion timescale $t_{\text{acc}} \propto 1/\dot{M}_*$: even at the same protostellar mass M_* , the evolutionary timescale is longer in the case of low \dot{M}_* . Therefore, the protostar has ample time to lose heat before gaining more mass. This results in the lower entropy and thus a smaller radius at the same protostellar mass in the low \dot{M}_* case as shown in the upper panel of Figure 7. Although with the smaller value, the overall evolutionary features of the high and low \dot{M}_* radii are similar.

Again, the protostellar evolution can be divided into four characteristic stages, i.e., (I) convection ($M_* \lesssim 3 M_\odot$), (II) swelling ($3 M_\odot \lesssim M_* \lesssim 4 M_\odot$), (III) KH contraction ($4 M_\odot \lesssim M_* \lesssim 7 M_\odot$), and (IV) main-sequence accretion ($M_* \gtrsim 7 M_\odot$) phases. Note that the first phase is now the convection phase instead of the adiabatic accretion. In the low \dot{M}_* case, the deuterium burning drastically affects the protostellar evolution in early phases (e.g., Stahler 1988). Since the evolution in the phases (III) and (IV) is similar to the previous high- \dot{M}_* case (§ 3.1), we emphasize the two early phases (I) and (II) in the following.

Convection Phase In the low \dot{M}_* case, the D burning begins in an earlier phase and has a more profound effect on the evolution than in the high- \dot{M}_* case (run MD3). As a result of the smaller radius, the temperature, as well as density, is higher in the low \dot{M}_* case (cf. lower panels of Fig. 2 and Fig. 7). The maximum temperature reaches 10^6 K as early as $M_* \simeq 0.2 M_\odot$ and active deuterium burning begins subsequently (Fig. 7), while in the high- \dot{M}_* case the D ignition does not occur until $M_* \simeq 6 M_\odot$ (Fig. 2). Unlike in the high- \dot{M}_* case, the deuterium burning makes most of the interior convective. This is a result of high density and thus high opacity at the ignition of deuterium burning, occurring at a fixed temperature of $\simeq 10^6$ K. Since high opacity hinders the radiative heat transport, entropy generated by deuterium burning cannot be transported radiatively. This necessarily gives rise to convection.

Figure 7 shows that the extent of the convective layers experiences a complicated history. At $M_* \simeq 0.3 M_\odot$, a convective layer appears for the first time slightly off-center. Inside the convective layer, entropy is homogenized and its value increases

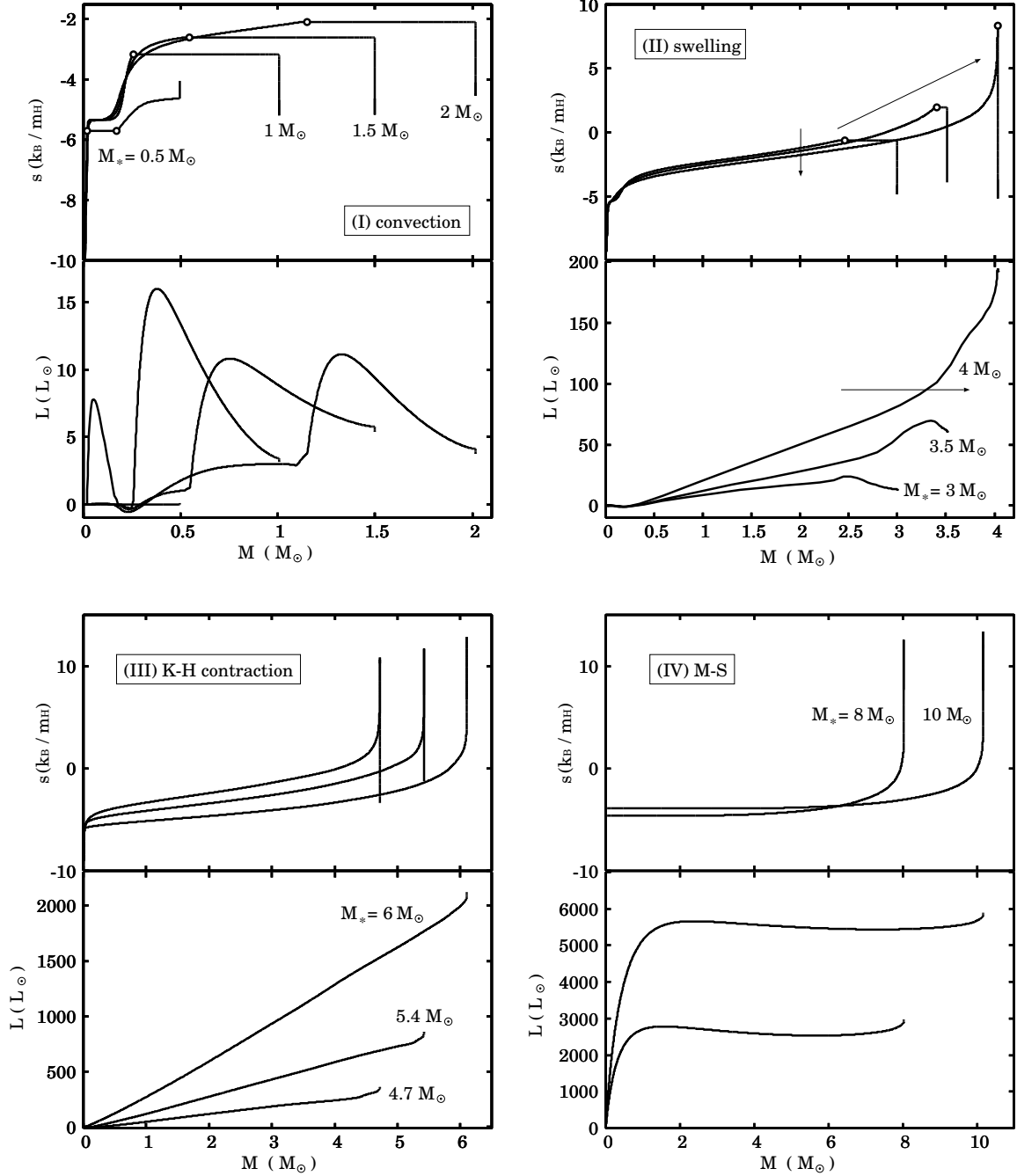


FIG. 8.— Same as Fig. 8 but for the lower accretion rate of $\dot{M}_* = 10^{-5} M_\odot/\text{yr}$ (run MD5).

owing to the D burning (Fig. 8, I). With this increased entropy, the outer layer is gradually incorporated into the convective region. Fresh deuterium is supplied from the newly incorporated layer and spreads over the convective region, and finally is consumed by nuclear burning at the bottom of the region. However, the expansion of the convective region cannot be maintained if the supply of deuterium becomes insufficient. Without the fuel, the deuterium concentration in the convective region $f_{d,cv}$ drops and the nuclear burning ceases: the convective region disappears. This occurs at $M_* \simeq 0.6 M_\odot$ (Fig. 7, upper). At $M_* \simeq 0.7 M_\odot$, another episode of deuterium burning begins just outside the first convective region, where fresh deuterium still remains. The second convective region develops there and immediately reaches the stellar surface. Although this complicated evolution of the convective regions is different from that reported in SST80b, this difference can be attributable to high sensitivity of the evolution on adopted initial deuterium abundance. We discuss this in greater details in Appendix B.1.

Since the energy generation by D burning is very sensitive to the temperature, temperature remains constant at $\simeq 1.5 \times 10^6 \text{K}$ during the active deuterium burning (Fig. 7, lower panel). This is the so-called thermostat effect (e.g.,

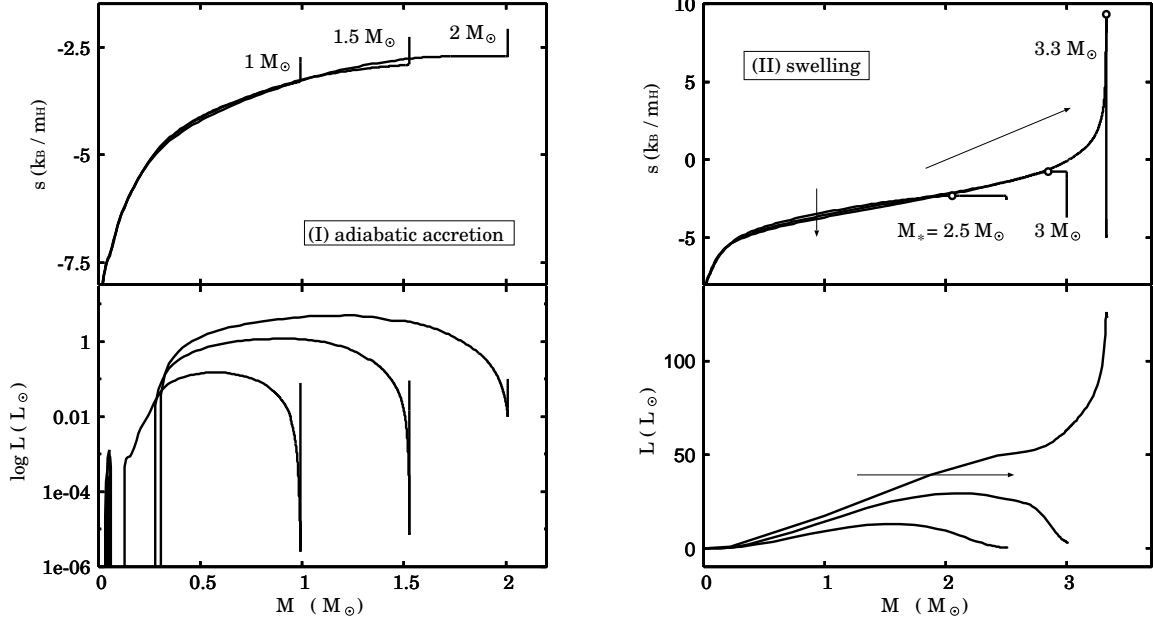


FIG. 9.— Same as Fig. 8 but for switching off deuterium burning in the calculation (run MD5-noD). Only profiles in the early adiabatic accretion phase and swelling phase are presented.

Stahler 1988). If this works, $M_*/R_* \propto T \simeq \text{const.}$ from equation (10): the protostellar radius R_* increases as $\propto M_*$. This linear increase in R_* with M_* can be observed in the range $0.7M_\odot \lesssim M_* \lesssim 1M_\odot$ (Fig. 7, upper panel).

When the deuterium concentration in the convective region drops to a few percent, the thermostat effect ceases to work. The maximum temperature starts increasing again and the radial expansion slows down after that. Owing to the high temperature, opacity decreases in the deep interior with increasing stellar mass. This allows efficient radiative energy transport and renders a large portion of the interior radiative. The radiative core gradually extends to the outer layer, and the convective layer moves outward. Since fresh deuterium is no longer supplied to the radiative interior by the mixing, deuterium is soon exhausted there. The expansion of the radiative interior occurs in a later phase in the calculation of PS91. This difference can be attributed to different initial models: whereas PS91 assumed a fully convective star of $1M_\odot$ as an initial model, we started calculation from the initial mass $M_{*,0} = 0.01M_\odot$. At $M_* = 1M_\odot$, the protostar is not fully convective in our case. The outer layers of $M > 0.25M_\odot$ are convective, where the D burning occurs at the bottom, while the remaining inner core is radiative at this moment. We confirmed that, starting from the same initial model, the

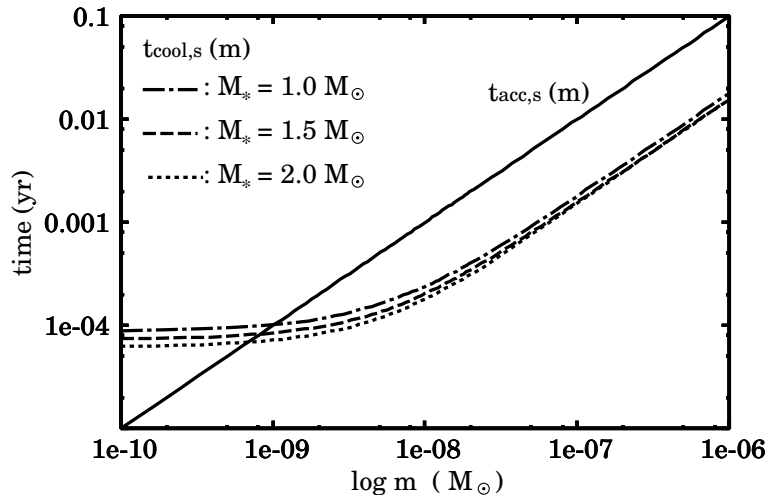


FIG. 10.— Same as Fig. 4 but for the case with the lower accretion rate of $\dot{M}_* = 10^{-5} M_\odot/\text{yr}$ and without deuterium burning (run MD5-noD). The local cooling timescales given by equation (5) at $M_* = 1.0$ (dot-dashed), 1.5 (dashed), and $2.0 M_\odot$ (dotted line) are presented.

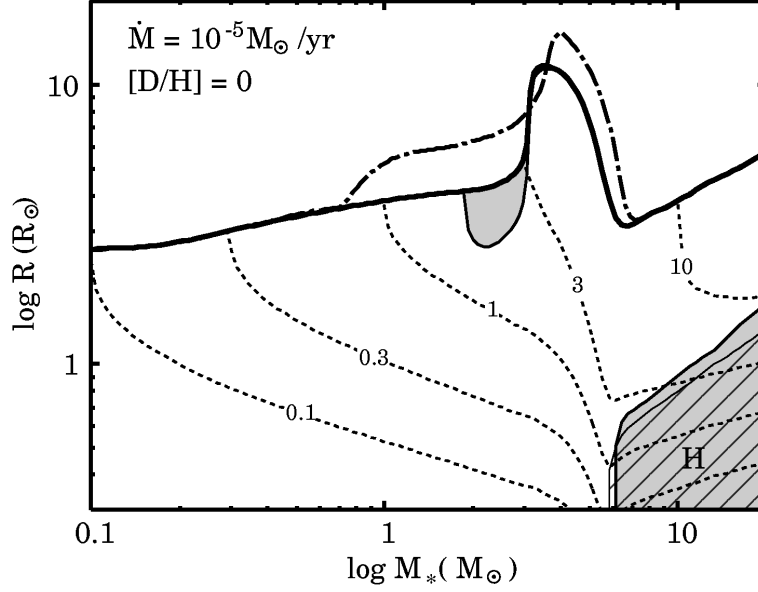


FIG. 11.— Same as the upper panel of Fig. 7 but for the case without the deuterium burning ($[D/H] = 0$, run MD5-noD). The dot-dashed line represents the mass-radius relation for the case with the fiducial deuterium abundance, $[D/H] = 2.5 \times 10^{-5}$ (run MD5, also see Fig. 7).

evolution becomes similar to that of PS91 as discussed in Appendix B.2.

Because of the early ignition of deuterium burning, entropy and luminosity profiles in this phase look rather different from those in the high \dot{M}_* case (see Fig. 3 and 8). For easier comparison, let us see the case without deuterium burning, where the similar profiles are in fact reproduced (Fig. 9). However, one important difference exists, the spiky structure in the entropy profiles near the surface. This shows significant entropy loss near the surface in the low \dot{M}_* case, which leads to the low entropy within the star. The reason can be seen clearly in Figure 10, where the comparison between the local accretion timescale $t_{\text{acc},s}$ and cooling timescale $t_{\text{cool},s}$ (eq.s 4 and 5) is presented. In contrast to the case of high \dot{M}_* , in most of the settling layer, $t_{\text{acc},s}$ is shorter than $t_{\text{cool},s}$: accreted matter loses entropy radiatively near the surface before settling into the adiabatic interior.

Swelling Phase In the short period of $3 M_\odot \lesssim M_* \lesssim 4 M_\odot$, the stellar radius jumps up by a factor of two. At the same time, the whole interior becomes radiative (Fig. 7, upper). Although deuterium burning continues near the surface, it does not drive convection any more.

The cause of this swelling has been attributed to the shell burning of deuterium, which also occurs in our calculation (Palla & Stahler 1990). However, we conclude that the main driver of the swelling is not the D shell burning, but the outward entropy transportation as in the case of the high accretion rate. The reasons are as follows. First, evolutionary features of entropy and luminosity profiles in this phase are similar to those in the swelling phase in the high \dot{M}_* case (run MD3; cf. Figs. 3, 8): in both cases, entropy decreases in the deep interior and increases significantly near the stellar surface; simultaneously, the peak of the luminosity distribution moves to the surface as the luminosity wave. Second, even in the run without deuterium burning (run MD5-noD), this swelling occurs as shown in Figure 11: the protostar swells up at $M_* \simeq 3 M_\odot$.

The interior luminosity L_* jumps up at $M_* \simeq 0.7 M_\odot$ with the arrival of the convective region at the surface as a result of high efficiency of convective heat transfer (Fig. 12, upper panel). Although this rise in L_* decreases t_{KH} , t_{KH} remains much longer than t_{acc} (Fig. 12, lower panel). It is not until another sudden rise in L_* at $\simeq 3 - 4 M_\odot$ due to the arrival of the luminosity wave that t_{KH} becomes as short as t_{acc} . The maximum radius is attained at this epoch since the swelling is also caused by the luminosity wave, as seen above. Then, the analytical argument leading to equation (12) also holds in this case: for $\dot{M}_* = 10^{-5} M_\odot/\text{yr}$, this leads to the maximum radius at $M_{*,\text{rmax}} \simeq 3.9 M_\odot$, which agrees with our numerical result.

Simultaneous returning to the radiative structure with the swelling has been explained by Palla & Stahler (1990). The luminosity from the steady deuterium burning is comparable to the accretion luminosity by chance:

$$L_{\text{D,st}} = \dot{M}_* \delta_{\text{D}} \sim \dot{M}_* \frac{GM_*}{R_*} = L_{\text{acc}}. \quad (15)$$

The epoch of the radial turn-around obeys equation (12), which is derived by equating t_{acc} and $t_{\text{KH,lmax}} = GM_*^2/R_*L_{\text{max}}$. This means that L_{max} becomes comparable to L_{acc} and thus to $L_{\text{D,st}}$ in the swelling phase. Hence, the radiative luminosity

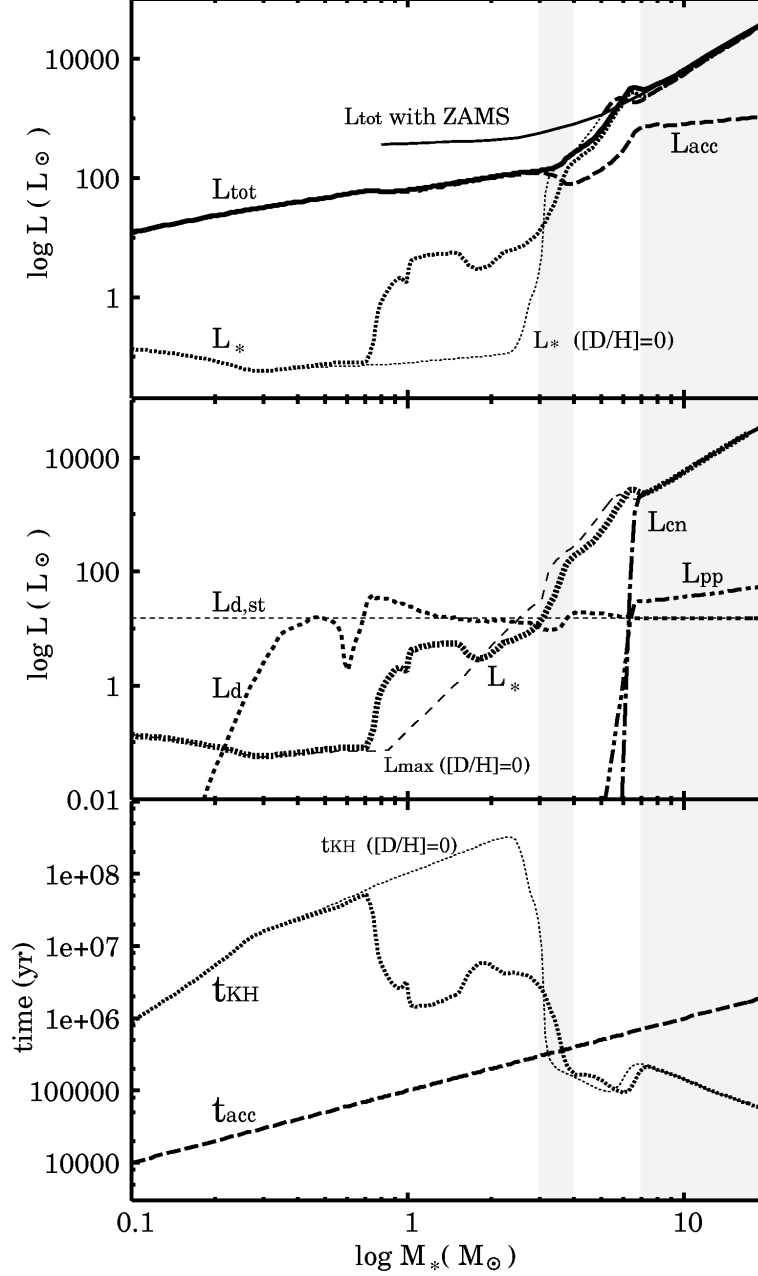


FIG. 12.— Same as Fig. 5 but for the lower accretion rate of $\dot{M}_* = 10^{-5} M_\odot/\text{yr}$ (run MD5). In each panel, the stellar luminosity L_* (Top panel, thin dotted line), maximum luminosity within the star L_{max} (Middle panel, thin coarse dashed line), and Kelvin-Helmholtz time t_{KH} (Bottom panel, thin dotted line) for the case without deuterium burning (run MD5-noD) are presented for comparison. In all panels, the shaded background shows the four characteristic phases, as in Fig. 7.

now has a capacity to transport the energy generated by deuterium burning: $L_{\text{max}} \sim L_{\text{D,st}}$. The deuterium burning no longer gives rise to any convective layer after the swelling.

Later Phases Subsequently, the protostar enters the KH contraction phase. The evolution thereafter is similar to the previous high- \dot{M}_* case. The maximum temperature within the star increases with the contraction, and hydrogen burning begins at $M_* \simeq 7 M_\odot$.

Evolution of the Radiative Precursor Figure 13 shows that the accretion flow is optically thin except in the early phase of $M_* < 1 M_\odot$ at the low accretion rate of $10^{-5} M_\odot/\text{yr}$. With the expansion at the active deuterium burning, the stellar surface emerges above the photosphere at $M_* \simeq 1 M_\odot$ and the radiative precursor disappears thereafter. Without

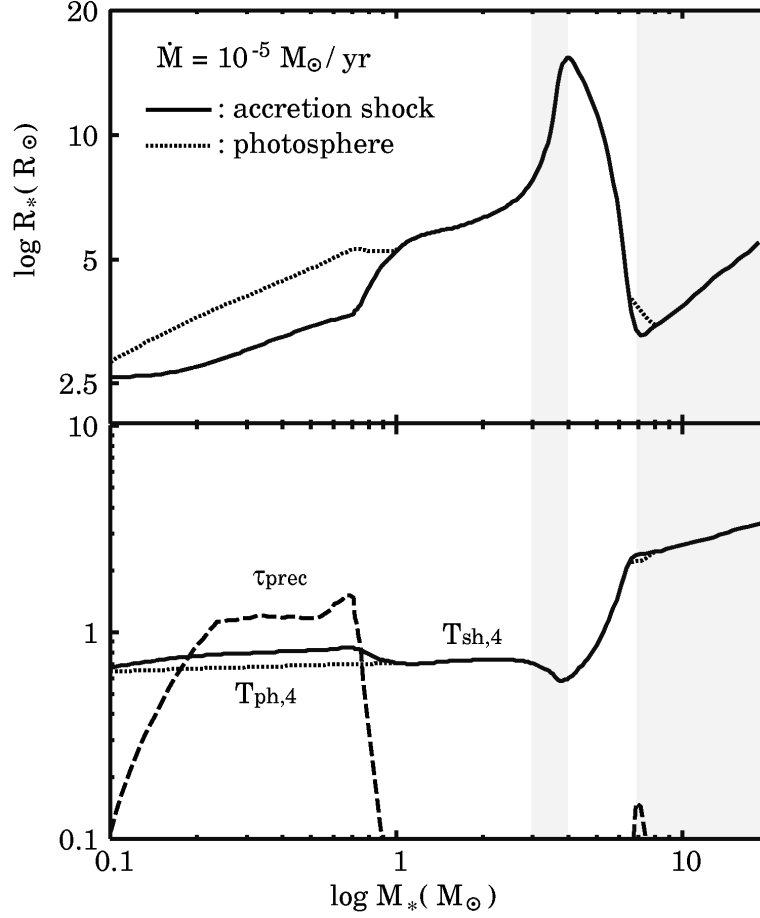


FIG. 13.— Same as Fig. 6 but for the lower accretion rate of $\dot{M}_* = 10^{-5} M_\odot/\text{yr}$ (run MD5). The shaded background shows the four characteristic phases, as in Fig. 7.

the precursor, the stellar surface is directly visible, with effective temperature rising remarkably in the KH contraction phase, i.e., for $M_* > 4M_\odot$. This is in stark contrast to the case of high accretion rate $10^{-3} M_\odot/\text{yr}$, where the effective temperature remains several thousand K throughout the evolution (Fig. 6).

3.3. Dependence on Mass Accretion Rates

Here, we summarize the effects of the different accretion rates on the protostellar evolution. The mass-radius relations of protostars with accretion rates $\dot{M}_* = 10^{-6}, 10^{-5}, 10^{-4}$, and $10^{-3} M_\odot/\text{yr}$ are shown in the upper panel of Figure 14.

First, the protostellar radius is larger for the higher accretion rate at the same protostellar mass, as discussed in § 3.1. For example, at $M_* = 1M_\odot$, the radius $R_* \simeq 25R_\odot$ for $10^{-3} M_\odot/\text{yr}$, while it is only $2.5R_\odot$ for $10^{-6} M_\odot/\text{yr}$. For easier comparison, the mass-radius relations in the no-deuterium cases are also shown by thin lines in Figure 14. The deuterium burning enhances the stellar radius, in particular, in low \dot{M}_* cases (see in this section below). Nevertheless, the trend of larger R_* for higher \dot{M}_* remains valid even without the deuterium burning. For simplicity, we do not include the effect of deuterium burning in the following argument. The origin of this trend is higher specific entropy for higher accretion rate. Recall that the stellar radius is larger with the high entropy in the stellar interior as shown by equation (8). The entropy distributions at $M_* = 1M_\odot$ for the no-D runs are shown in Figure 15, which indeed demonstrates that the entropy is higher for the higher \dot{M}_* cases. The interior entropy is set in the post-shock settling layer where radiative cooling can reduce the entropy from the initial post-shock value as observed in spiky structures near the surface (e.g., the case of $\dot{M}_* \lesssim 10^{-5} M_\odot/\text{yr}$ in Fig. 15). For efficient radiative cooling, the local cooling time $t_{\text{cool},s}$ in the settling layer must be shorter than the local accretion time $t_{\text{acc},s}$, as explained in § 3.1 and 3.2. Figure 16 shows that the ratio $t_{\text{cool},s}/t_{\text{acc},s}$ is smaller for lower \dot{M}_* and becomes less than unity for $\lesssim 10^{-5} M_\odot/\text{yr}$. Thus the accreted gas cools radiatively in the settling layer in low \dot{M}_* ($\lesssim 10^{-5} M_\odot/\text{yr}$) cases, while in the higher \dot{M}_* cases, the gas is embedded into the stellar interior without losing the post-shock entropy. The difference in entropy among high \dot{M}_* ($\gtrsim 10^{-4} M_\odot/\text{yr}$) cases comes from the higher post-shock entropy for higher \dot{M}_* . In those cases, the protostar is enshrouded with the radiative precursor, whose

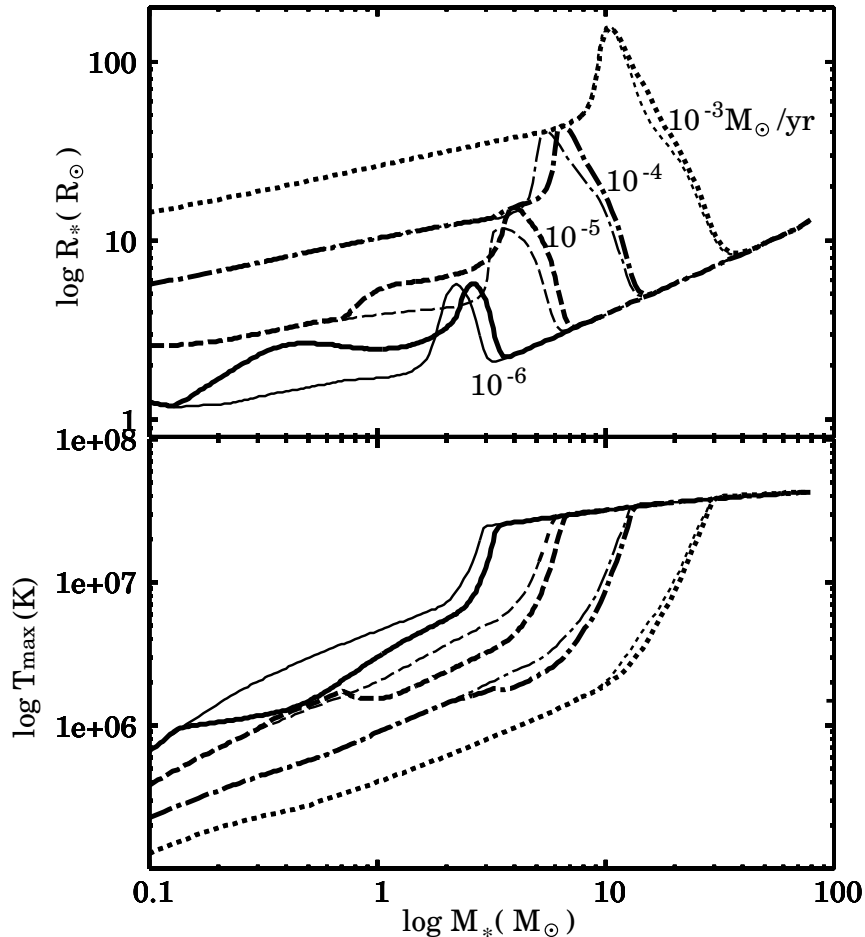


FIG. 14.— Evolution of the protostellar radii (upper panel) and the maximum temperatures within the stars (lower panel) for different mass accretion rates. The cases of $\dot{M}_* = 10^{-6}$ (run MD6; solid), 10^{-5} (MD5; dashed), 10^{-4} (MD4; dot-dashed), and $10^{-3} M_\odot/\text{yr}$ (MD3; dotted line) are depicted. Also shown by the thin lines are the runs without deuterium burning (“noD” runs) for the same accretion rates. In both panels, all the curves finally converge to single lines, which is the relations for the main-sequence stars.

optical depth is larger for the higher accretion rate (c.f., Figs. 6 and 13, bottom). Consequently, more heat is trapped in the precursor, which leads to the higher post-shock entropy.

Figure 14 shows not only that not only the swelling of the stellar radius occurs even in the “no-D” runs, but also that their timings are almost the same as in the cases with D. This supports our view that the cause of the swelling is outward entropy transport by the luminosity wave rather than the deuterium shell-burning (§ 3.1 and 3.2). Also, in all cases, the epoch of the swelling obeys equation (12), which is derived by equating the accretion time t_{acc} and the KH time $t_{\text{KH}, \text{lmax}}$.

Another clear tendency is that the deuterium burning begins at higher stellar mass for higher accretion rate. Similarly, the onset of hydrogen burning and subsequent arrival at the ZAMS are postponed until higher protostellar mass for the higher accretion rate. For example, the ZAMS arrival is at $M_* \simeq 4M_\odot$ ($40M_\odot$) for 10^{-6} (10^{-3} , respectively) M_\odot/yr . These delayed nuclear ignitions reflect the lower temperature within the protostar for the higher \dot{M}_* at the same M_* (Fig. 14, lower panel). Since R_* is larger with higher \dot{M}_* at a given M_* , typical temperature is lower within the star. Substituting numerical values in equation (10), we obtain

$$T_{\text{max}} \sim 10^7 \text{ K} \left(\frac{M_*}{M_\odot} \right) \left(\frac{R_*}{R_\odot} \right)^{-1}, \quad (16)$$

which is a good approximation for our numerical results.

Finally, we consider the significance of deuterium burning for protostellar evolution. Comparing with “no-D” runs, we find that the effect of deuterium burning not only appears later, but also becomes weaker with increasing accretion rates. At the low accretion rates $\dot{M}_* \leq 10^{-5} M_\odot/\text{yr}$, convection spreads into a wide portion of the star owing to the vigorous deuterium burning. In addition, the thermostat effect works and the stellar radius increases linearly during this period. At the higher accretion rates $\dot{M}_* \geq 10^{-4} M_\odot/\text{yr}$, on the other hand, deuterium burning affects the protostellar evolution only slightly. Convective regions do not appear even after the beginning of deuterium burning for $\dot{M}_* = 10^{-3} M_\odot/\text{yr}$

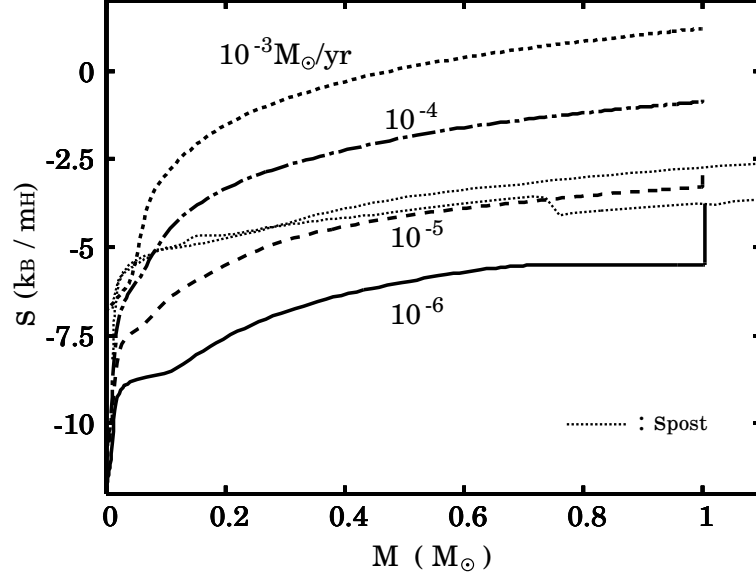


FIG. 15.— Distributions of the specific entropy for the case without deuterium (“no-D” runs in Table 1) at the epoch of $M_* = 1 M_\odot$ for different accretion rates. Histories of the post-shock values are also plotted by the dotted lines for the cases with $\dot{M}_* = 10^{-6}$ and $10^{-5} M_\odot/\text{yr}$. For the cases with $\dot{M}_* = 10^{-4}$ and $10^{-3} M_\odot/\text{yr}$, those curves completely overlap with the entropy distributions at $M_* = 1 M_\odot$.

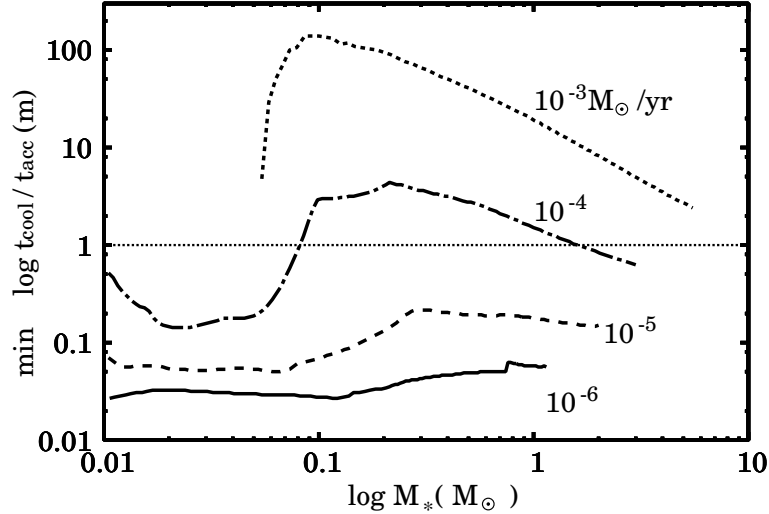


FIG. 16.— Evolution of the minimum value of the ratio $t_{\text{cool},s}(m)/t_{\text{acc},s}(m)$ in the surface settling layer. The no-D cases are shown for $\dot{M}_* = 10^{-6}$ (solid), 10^{-5} (dashed), 10^{-4} (dot-dashed), and $10^{-3} M_\odot/\text{yr}$ (dotted). For the ratio $t_{\text{cool},s}(m)/t_{\text{acc},s}(m)$ exceeding unity, the accreted material settles into the interior without losing its post-shock entropy radiatively.

(§ 3.1).

A key quantity for understanding this variation is the maximum radiative luminosity at the ignition of deuterium burning. The maximum radiative luminosity within the star L_{max} at deuterium ignition can be evaluated by eliminating R_* and M_* in equation (11) with (9), (16), and setting $T_{\text{max}} \sim 10^6$ K:

$$L_{\text{max}} \sim 10^3 L_\odot \left(\frac{\dot{M}_*}{10^{-3} M_\odot/\text{yr}} \right)^{2.8}. \quad (17)$$

On the other hand, the luminosity from deuterium burning is (eq. 13) $L_{\text{D,st}} \sim 10^3 L_\odot (\dot{M}_*/10^{-3} M_\odot/\text{yr})$. For accretion rate $\dot{M}_* \geq 10^{-3} M_\odot/\text{yr}$, $L_{\text{max}} > L_{\text{max,D}}$: radiation is able to carry away all the entropy generated by the deuterium burning. Therefore, the protostellar interior remains radiative in the high \dot{M}_* cases (e.g., run MD3, see § 3.1), while

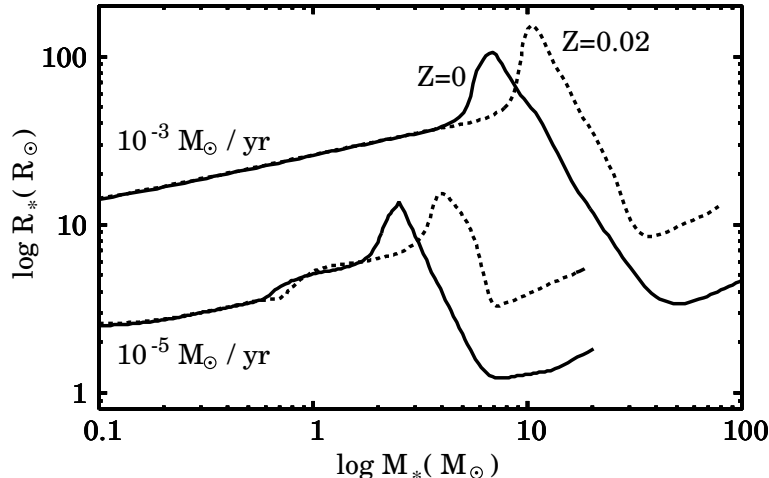


FIG. 17.— The protostellar mass-radius relations for different metallicities. The cases of the solar (dotted; runs MD5 and MD3) and zero (solid; MD5-z0 and MD3-z0) metallicities are presented for the accretion rates $\dot{M}_* = 10^{-5}$ and $10^{-3} M_\odot/\text{yr}$.

convection is excited for the lower \dot{M}_* (e.g., run MD5, see § 3.2).

3.4. Comparison with Primordial Star Formation

Besides the massive star formation in the local universe, high accretion rates have been invoked in the primordial star formation in the early universe. Without important metal coolants, the temperature remains at several hundred K in the primordial gas (e.g., Saslaw & Zipoy 1967; Matsuda, Sato & Takeda 1969; Palla, Salpeter & Stahler 1983). The accretion rate, which is given by

$$\dot{M}_* \simeq \frac{c_s^3}{G} = 10^{-3} M_\odot/\text{yr} \left(\frac{T}{500\text{K}} \right)^{3/2}, \quad (18)$$

where c_s and T are the sound speed and temperature, respectively, in star-forming clouds, becomes as high as $10^{-3} M_\odot/\text{yr}$ even without turbulence (SPS86). As a result of similar accretion rates, protostellar evolution of the primordial stars well resembles with those of the high \dot{M}_* cases studied in this paper (SPS86; Omukai & Palla 2001, 2003). The mass-radius relations for the primordial ($Z = 0$) protostars are presented in Figure 17, along with their solar-metallicity ($Z = 0.02$) counterparts for comparison. This indicates that basic evolutionary features are similar despite differences in metallicity: as in the present-day protostars, primordial protostars pass through the same four characteristic phases (see § 3.1 and 3.2). The following two differences, however, still exist. First, the swelling of the protostar and subsequent transition to the KH contraction occur earlier in the $Z = 0$ cases. For example, for $\dot{M}_* = 10^{-3} M_\odot/\text{yr}$, the maximum radius is attained and the KH contraction begins at $10 M_\odot$ in the $Z = 0.02$ case, while it is $7 M_\odot$ in the $Z = 0$ case. Recall that the transition to those phases is caused by the decrease in opacity with increasing M_* (§ 3.1). Owing to the lack of heavy elements, the opacity is lower in the primordial gas at the same density and temperature. Efficient radiative heat transport begins earlier, which results in the earlier transitions in the evolutionary phases. Second, the stellar radius in the main-sequence phase is smaller as a result of higher interior temperature ($\simeq 10^8 \text{K}$) for the primordial stars. Due to the lack of C and N, sufficient energy production by the CN cycle is not available at a temperature similar to that of the solar metallicity case ($\simeq 10^7 \text{K}$). The KH contraction is not halted until the temperature reaches $\simeq 10^8 \text{K}$, where a small amount of carbon produced by the He burning enables the operation of the CN cycle (Ezer & Cameron 1971; Omukai & Palla 2003). Since more contraction is needed, the arrival at the ZAMS can be later in the $Z = 0$ case, despite the earlier beginning of the KH contraction: for example, it is $30 M_\odot$ ($50 M_\odot$) in the Z_\odot ($Z = 0$, respectively) case.

3.5. Radiation Pressure Barrier on the Accreting Gas Envelope

The higher the mass accretion rate, the more massive the protostar grows before the arrival at the ZAMS phase (§ 3.1 and 3.3). However, this trend does not continue unlimitedly: for a rate exceeding a threshold value, stars have an upper mass limit set by the radiation pressure onto the radiative precursor.

The evolution of the protostellar radius is shown in Figure 18 (upper panel) for cases with very high accretion rates $> 10^{-3} M_\odot/\text{yr}$. Up to a certain moment in the KH contraction phase, the evolution in all cases proceeds in a qualitatively similar way although the radius is larger and the onset of swelling and the KH contraction are later for higher \dot{M}_* cases. However, for accretion rates $\dot{M}_* > 3 \times 10^{-3} M_\odot/\text{yr}$, the contraction is halted at $\simeq 40 M_\odot$, followed by abrupt expansion at $\simeq 50 M_\odot$. In such cases, further steady accretion onto the star is not possible owing to strong radiative

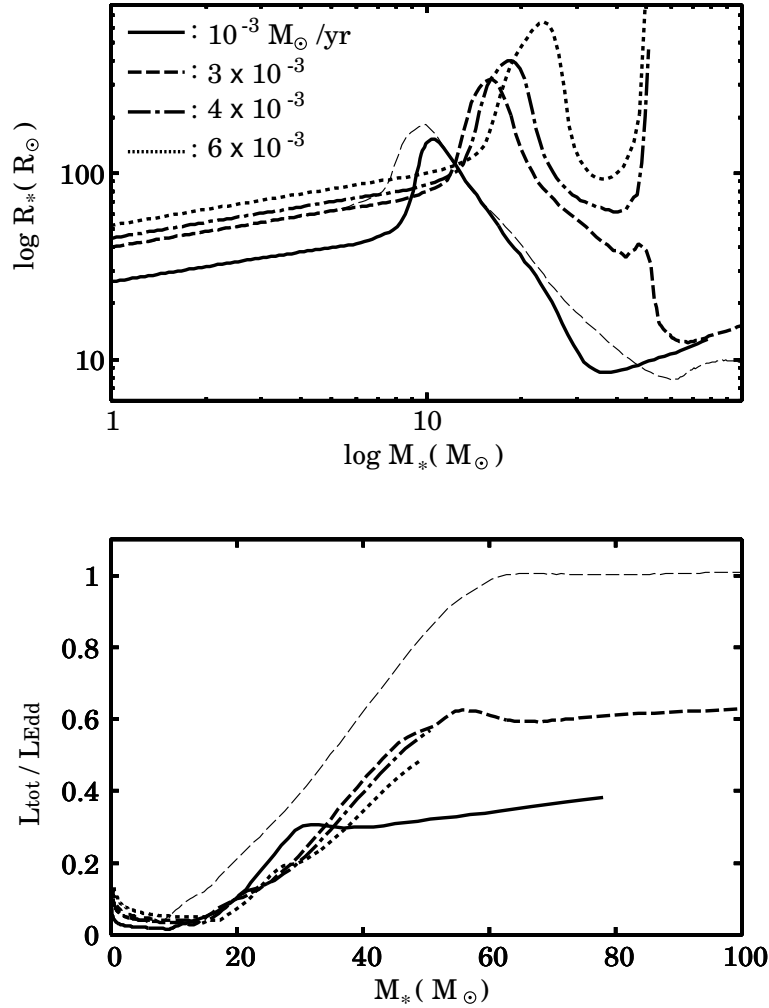


FIG. 18.— *Upper panel*: Evolution of the protostellar radii for cases at the very high accretion rates of 10^{-3} (solid, run MD3), 3×10^{-3} (dashed, MD3x3), 4×10^{-3} (dot-dashed, MD4x3), and $6 \times 10^{-3} M_\odot/\text{yr}$ (dotted, MD6x3). For comparison, we also plot the case of a primordial ($Z = 0$) protostar with $3 \times 10^{-3} M_\odot/\text{yr}$ (thin dashed, MD3x3-z0). *Lower panel*: Evolution of a ratio between the total luminosity of protostars and Eddington luminosity for the same cases.

pressure exerted onto the radiative precursor. This phenomenon has been found for the primordial star formation by Omukai & Palla (2001, 2003). They found that abrupt expansion occurs when the total luminosity from a protostar, $L_{\text{tot}} = L_* + L_{\text{acc}} = L_* + GM_*\dot{M}_*/R_*$, becomes close to the Eddington luminosity L_{Edd} . The strong radiation pressure decelerates the accretion flow and then reduces the ram pressure onto the stellar surface. With reduced inward ram pressure, an outward thrust by the interior radiation blows a thin surface layer away.

The critical accretion rate \dot{M}_* is defined as the rate above which the abrupt stellar expansion occurs in the KH contraction phase. By using the condition that L_{tot} reaches L_{Edd} before the protostar reaches the ZAMS, (Omukai & Palla 2003) derived the critical rate as follows:

$$L_{\text{ZAMS}} + \frac{GM_{\text{ZAMS}}\dot{M}_{*,\text{cr}}}{R_{\text{ZAMS}}} = L_{\text{Edd}}, \quad (19)$$

that is,

$$\dot{M}_{*,\text{cr}} = \frac{4\pi c R_{\text{ZAMS}}}{\kappa_{\text{esc}}} \left(1 - \frac{L_{\text{ZAMS}}}{L_{\text{Edd}}} \right), \quad (20)$$

where κ_{esc} is the electron-scattering opacity, and the suffix “ZAMS” means quantities of the ZAMS stars. Although the critical rate $\dot{M}_{*,\text{cr}}$ by equation (20) depends on the stellar mass, the dependence is very weak and $\dot{M}_{*,\text{cr}} \simeq 4 \times 10^{-3} M_\odot/\text{yr}$ for the primordial stars. Since the ZAMS radius increases with metallicity (see § 3.4), $\dot{M}_{*,\text{cr}}$ is expected to increase with metallicity. For example, for $Z = 10^{-4}$, $\dot{M}_{*,\text{cr}} = 9 \times 10^{-3} M_\odot/\text{yr}$ by equation (20), and the evolutionary calculation demonstrated that abrupt stellar expansion occurs in fact for higher accretion rates (Omukai & Palla 2003).

Our calculations, however, indicate that the critical accretion rate in the solar metallicity case is $\simeq 3 \times 10^{-3} M_{\odot}/\text{yr}$, slightly smaller than that of primordial protostars. This apparent contradiction comes from the fact that, in the solar metallicity case, opacity in the accreting envelope is higher than that of the electron scattering one κ_{es} postulated in the above derivation for the critical accretion rate. In fact, the violent stellar expansion is found to take place with a total luminosity of about a half of the Eddington luminosity, as shown in the lower panel of Figure 18. A marginal case is Run MD3x3, where the contraction is about to be reversed, but the star barely reaches the ZAMS after some loitering. In this case, the Eddington ratio $f_{\text{Edd}} = L_{\text{tot}}/L_{\text{Edd}}$ slightly exceeds 0.5 at $M_* \simeq 45 M_{\odot}$. For comparison, the case of the primordial star is shown for the same accretion rate, $\dot{M}_* = 3 \times 10^{-3} M_{\odot}/\text{yr}$, which is slightly lower than the critical accretion rate (run MD3x3-z0). Because of the earlier transition to the KH contraction phase, the Eddington ratio also begins to increase earlier than the present-day counterpart (run MD3x3). Despite high luminosity almost reaching the Eddington limit, the KH contraction is not reversed and the protostar can grow further. Taking into account the higher opacity in the envelope, we add the Eddington factor of 0.5 to equation (19):

$$L_{\text{ZAMS}} + \frac{GM_{\text{ZAMS}}\dot{M}_{*,\text{cr}}}{R_{\text{ZAMS}}} \simeq 0.5L_{\text{Edd}} \quad (21)$$

for present-day protostars. The critical accretion rate becomes $\dot{M}_{*,\text{cr}} \simeq 3 \times 10^{-3} M_{\odot}/\text{yr}$, which agrees well with our numerical results. Although this critical rate is a function of the stellar mass, its dependence is weak as in the primordial case.

Our results suggest an upper mass limit of PMS stars at $\simeq 60 M_{\odot}$, which corresponds to the mass where the protostar reaches the ZAMS at the critical accretion rate of $\dot{M}_{\text{cr}} \sim 3 \times 10^{-3} M_{\odot}/\text{yr}$. More massive PMS stars cannot be formed by steady mass accretion. With higher accretion rates, the steady accretion is halted by the abrupt expansion at $M_* \simeq 50 M_{\odot}$. What happens after the abrupt expansion is speculated upon in the next section.

4. UPPER LIMIT ON THE STELLAR MASS BY RADIATION FEEDBACK

As long as the central star is not so massive and its feedback on the accreting envelope is weak, the accretion proceeds at a rate set by the condition of the parent star-forming core. Our assumption concerning the accretion at a pre-determined rate remains valid. However, when the central star grows massive enough and its feedback, e.g. radiative pressure on the dusty outer envelope, thermal pressure in the HII region, etc., can no longer be neglected, the accretion rate is now regulated by the stellar feedback. The mass accretion is eventually terminated and the final stellar mass is set at this moment.

Among possible types of feedback, the radiation pressure on the outer dusty envelope is considered to be the most important in terminating the protostellar accretion (e.g., WC87). Since no such outer envelope has been included in our calculation, we evaluate here the epoch of accretion termination by stellar feedback with the assumption that the accretion rate is roughly constant up to this moment.

Most of the stellar radiation, emitted in the optical or UV range, is absorbed in a thin innermost layer of the dusty envelope, i.e., the dust destruction front, and the outward momentum of photons is transferred to the flow (see Fig. 1). Overcoming this radiation pressure barrier is a necessary condition for continuing accretion. The condition that the outward radiation pressure falls below the inward ram pressure of the accretion flow is expressed as

$$\frac{L_{\text{tot}}}{4\pi R_{\text{d}}^2 c} < \rho u^2, \quad (22)$$

where R_{d} is the radius of the dust destruction front, and ρ and u are the flow density and velocity there. The limit on the stellar mass by this condition is shown in Figure 19 as a function of the mass accretion rate (i.e., “ P_{ram} limit”). Here, we have assumed that the flow is in the free-fall. In Figure 19, the epochs of the maximum swelling and the arrival at the ZAMS are also presented from our results. Except in cases with very high accretion rates ($> 3 \times 10^{-3} M_{\odot}/\text{yr}$; § 3.5), the radiation pressure limit is attained after the stars reach the ZAMS. This verifies previous authors’ treatment in assuming that the central star is already in the ZAMS phase when the feedback becomes important (e.g., WC87).

In reality, the accretion flow is decelerated before reaching the dust destruction front. The radiation absorbed at the dust destruction front is re-emitted in infrared wavelengths and this re-emitted radiation imparts pressure onto the outer flow. This radiation pressure exceeds the gravitational pull of the star if the luminosity exceeds (McKee & Ostriker 2007):

$$L_{\text{Edd,d}} = \frac{4\pi cGM_*}{\kappa_{\text{d,IR}}} \simeq 1600L_{\odot} \left(\frac{M_*}{M_{\odot}} \right), \quad (23)$$

which is the “Eddington luminosity” for dusty gas, calculated by using the dust opacity for the far-infrared light $\kappa_{\text{d,IR}} \simeq 8 \text{ cm}^2/\text{g}$ instead of the electron-scattering opacity. The adopted value $8 \text{ cm}^2/\text{g}$ is the Rosseland mean opacity at $T \simeq 600 \text{ K}$, where the opacity takes the maximum value (Pollack et al. 1994). In the outermost region of the dust cocoon, where $T < 600 \text{ K}$ and $\kappa_{\text{d,IR}} < 8 \text{ cm}^2/\text{g}$, the deceleration effect is somewhat milder. This effect becomes significant when the flow reaches the inner warm region. As shown by the light-shaded region in Figure 19, the deceleration of dusty flow occurs ($L_{\text{tot}} > L_{\text{Edd,d}}$) in a wide range of M_* and \dot{M}_* . In this case, the upper mass limit by the radiation pressure (“ P_{ram} limit” in Fig. 19), which is derived by assuming the free-fall flow, becomes lower: the boundary of the “ P_{ram} limit” region shifts to the left to some extent. To evaluate this effect more quantitatively and then to identify how mass accretion is finally terminated, further studies will be needed. It has been shown that the deceleration effect of infrared light is diminished by

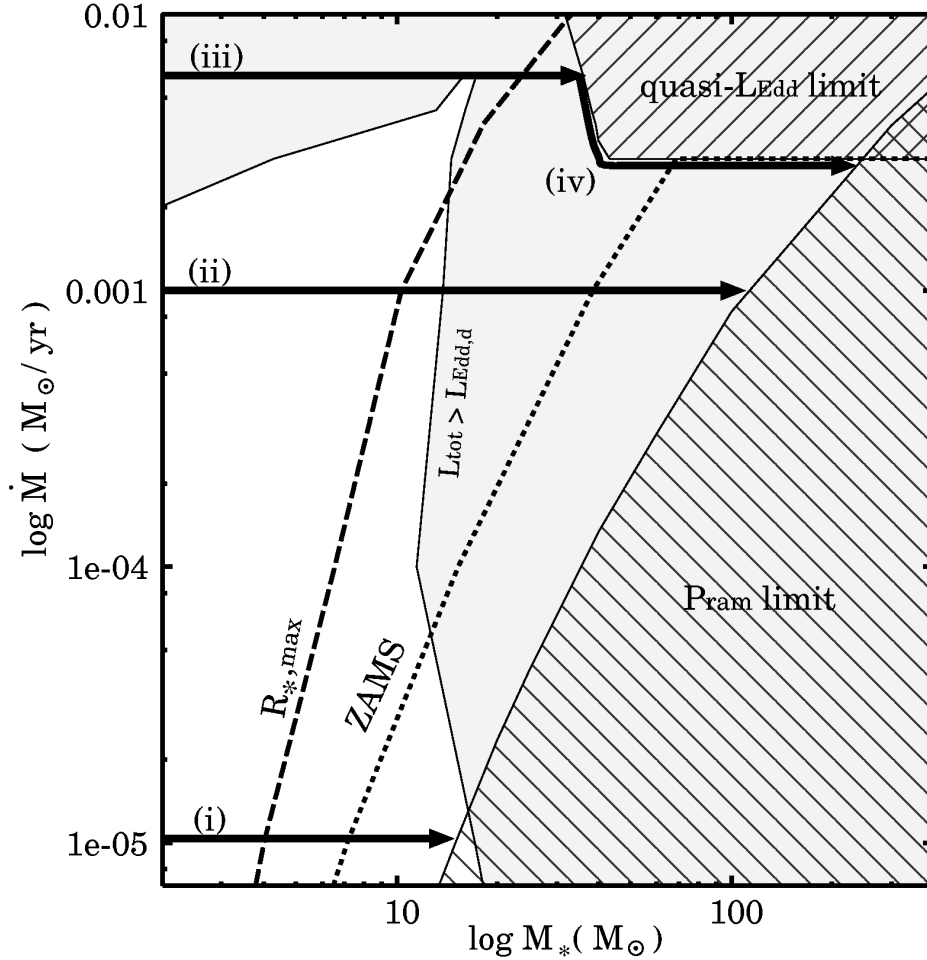


FIG. 19.— Limits on the stellar mass for each accretion rate by various feedback effects. The three horizontal arrows represent protostellar evolution at the accretion rate of (i) $\dot{M}_* = 10^{-5}$ (run MD5), (ii) 10^{-3} (run MD3), and (iii) $6 \times 10^{-3} M_\odot/\text{yr}$ (run MD6x3). Also shown are the stellar masses where the protostellar radii reach the maximum (dashed line) and where the protostars arrive at the ZAMS (dotted line). The region shaded by light gray represents where the total luminosity of the protostar, $L_{\text{tot}} = L_* + L_{\text{acc}}$ exceeds the dust Eddington luminosity $L_{\text{Edd,d}}$, given by equation (23). The lower-right hatched region represents where the ram pressure of the free-fall flow is insufficient to overcome the radiation pressure barrier at the dust destruction front. The upper-right hatched region denotes the similar prohibited region but for the radiation pressure acting on a gas envelopes just around the protostar. The extra arrow (iv) indicates a possible path along which the protostar will evolve after the gas envelope is disrupted by the radiation pressure (see text).

reduced dust opacity (WC87), non-spherical accretion (e.g., Nakano 1989; Yorke & Sonnhalter 2002), and other various processes (e.g., see McKee & Ostriker 2007 for a recent review). Note that even with the reduced dust opacity, the “ P_{ram} limit” still remains as long as the dusty envelope is thick enough for optical/UV (not infrared) light from the star.

As seen in § 3.5, for a very high accretion rate of $\dot{M}_* > 3 \times 10^{-3} M_\odot/\text{yr}$, the radiation pressure acting on the gas envelope terminates the steady mass accretion. Figure 19 shows that this limit (“quasi- L_{Edd} limit”) is more severe than the radiation pressure limit for $\dot{M}_* > 3 \times 10^{-3} M_\odot/\text{yr}$ although the deceleration of the dusty flow is already important. Note that WC87’s result on this quasi-Eddington limit differs from ours (see their Fig. 5). This discrepancy comes from their assumption that the forming star is already in the ZAMS, which is not valid in that case. On the other hand, we have consistently calculated the evolution until this limit is reached and the star begins abrupt expansion. For such a high accretion rate, what happens when the steady accretion becomes impossible is not clear in realistic situations. The accreting envelope may be completely blown away and growth of the protostar may be terminated at this point. Without accretion, the protostar quickly relaxes to a ZAMS star. Another possibility is that since the strong radiation force originates in the accretion luminosity itself, the accretion may continue in a self-regulated way by reducing its rate, for example, by an outflow. This process may proceed in a sporadic way: the protostar continues to grow alternately repeating eruption and accretion. If this is the case, the protostar evolves along the trajectory (iv) in Figure 19, which runs along the boundary of the prohibited region and the maximum stellar mass is about $250 M_\odot$ set by the radiation pressure feedback at the critical accretion rate $\dot{M}_{*,\text{cr}} \simeq 3 \times 10^{-3} M_\odot/\text{yr}$ (Fig. 19). This is a somewhat higher value than the likely upper mass cut-off of the Galactic initial mass function $\sim 150 M_\odot$ (e.g., Weidner & Kroupa 2004; Figer 2005).

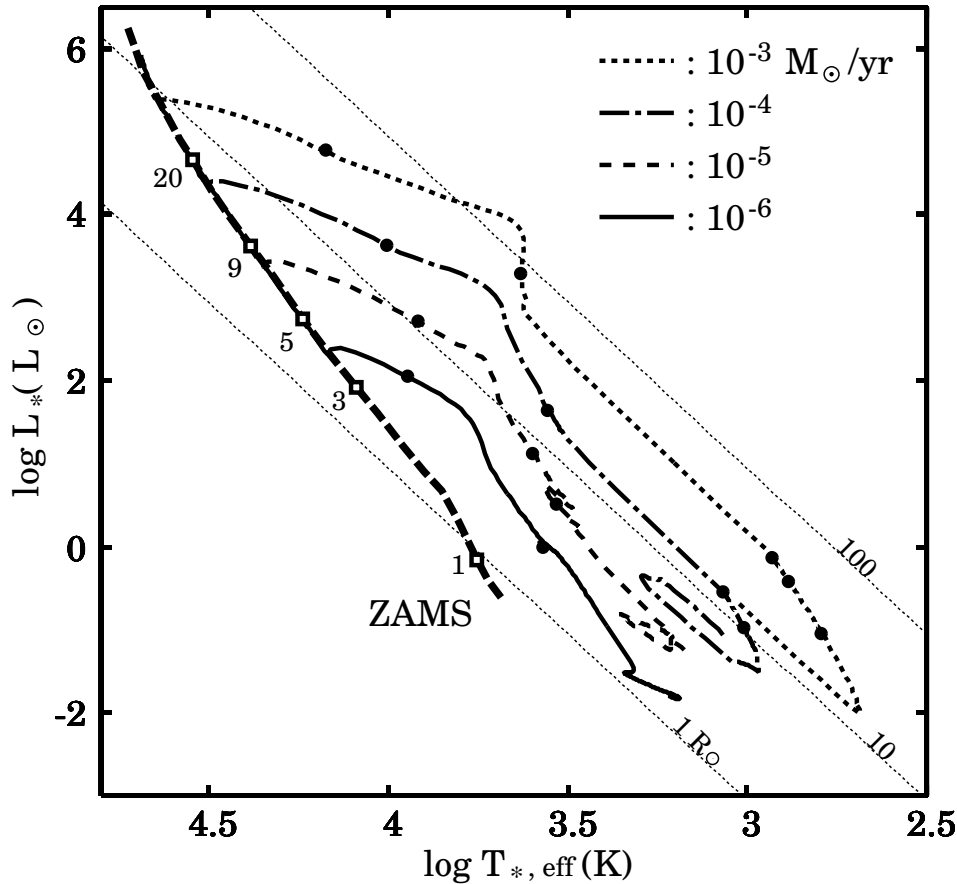


FIG. 20.— The stellar birthlines for different accretion rates. The cases for accretion rates $10^{-6} M_{\odot}/\text{yr}$ (solid; run MD6), 10^{-5} (dashed; MD5), 10^{-4} (dot-dashed; MD4), and $10^{-3} M_{\odot}/\text{yr}$ (dotted; MD3) are presented. Each track shows the evolution from the initial model, and filled circles on the track represent points of the stellar mass $M_{*} = 1, 3, 5, 9,$ and $20 M_{\odot}$ from the lower right in this order. The thick broken line represents the positions for zero-age main-sequence from Schaller et al. (1992). The open squares along the line denote the positions for the same masses as above. The dotted straight lines indicate the loci for the constant stellar radius of $1 R_{\odot}, 10 R_{\odot},$ and $100 R_{\odot}$.

This disagreement might be due to the deceleration of the outer dusty envelope, which is not included in this analysis.

5. OBSERVATIONAL SIGNATURES OF HIGH ACCRETION RATES

Massive protostars with high accretion rates have some characteristic observational features. In this section, we explore possibilities of identifying them observationally and of verifying the postulated high accretion rates. Although protostars still in the main accretion phase are hard to observe directly, pre-main sequence (PMS) stars just after this phase are optically visible. The distribution of such PMS stars in the Hertzsprung-Russell (HR) diagram retains a footprint of the previous accretion phase. The birthline is the initial loci of the PMS stars on the HR diagram as a function of the stellar mass. The PMS stars move down-left toward the ZAMS line on the diagram thereafter. It has been shown that the birthline for $\dot{M}_{*} \sim 10^{-5} M_{\odot}/\text{yr}$ successfully traces the upper envelope of observed distributions of low-mass and intermediate-mass PMS stars in the HR diagram (Palla & Stahler 1992; Norberg & Maeder 2000). In Figure 20, we show the birthlines for various accretion rates. These tracks are calculated from the interior luminosity L_{*} and the stellar radius R_{*} at the end of the accretion, i.e., when the protostellar mass reaches M_{*} . Without the accretion, contribution to the total luminosity is now only by the interior one L_{*} and the effective temperature is given by $T_{*,\text{eff}} \equiv (L_{*}/4\pi\sigma R_{*}^2)^{1/4}$. With higher \dot{M}_{*} , protostars have larger radii and their birthline shifts toward the upper-right. This dependence on \dot{M}_{*} is consistent with previous calculations (Palla & Stahler 1992; Norberg & Maeder 2000).

If a high accretion rate of $\dot{M}_{*} > 10^{-4} M_{\odot}/\text{yr}$ is indeed achieved in massive star formation, stars as massive as $10 M_{\odot}$ have not yet arrived at the ZAMS at the end of the accretion phase. Thus, the presence of such massive PMS stars is peculiar to the high \dot{M}_{*} scenario. These PMS stars are very luminous with $L_{*} > 10^4 L_{\odot}$, and their effective temperature is much lower than that of the ZAMS stars. Although some candidates have been reported very close to the ZAMS line, no such object has yet been firmly detected (e.g., Hanson, Howarth & Conti 1997). One explanation for the lack of detection is the very short KH timescale t_{KH} of such PMS stars. For example, in the case with $\dot{M}_{*} = 10^{-3} M_{\odot}/\text{yr}$ (run MD3), t_{KH}

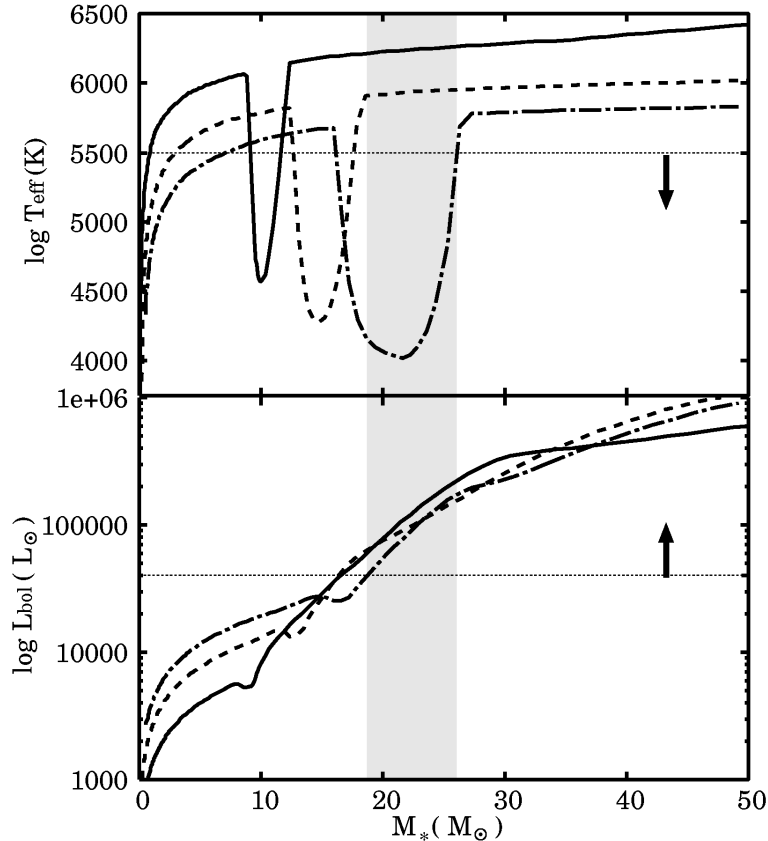


FIG. 21.— Evolution of the effective temperatures and bolometric luminosities of protostars with accretion rate $\dot{M}_* = 10^{-3}$ (solid; run MD3), 3×10^{-3} (dashed; MD3x3), and $6 \times 10^{-3} M_\odot/\text{yr}$ (dot-dashed; MD6x3). The condition required for the protostar in Orion KL region (Morino et al. 1998) is indicated by the horizontal lines with arrows; $L_{\text{tot}} \geq 4 \times 10^4 L_\odot$ and $T_{\text{eff}} < 5500\text{K}$. The mass range satisfying this condition is denoted by the shade for the case of $\dot{M}_* = 6 \times 10^{-3} M_\odot/\text{yr}$.

falls below 10^4yr for $M_* > 10 M_\odot$ (Fig. 5, bottom). On the other hand, from the case with $\dot{M}_* = 10^{-5} M_\odot/\text{yr}$ (run MD5) we see that $t_{\text{KH}} > 10^6 \text{yr}$ (10^5yr) for low- (intermediate-, respectively) mass protostars (Fig. 12, bottom). In addition to the small number of massive stars, such a short duration in the PMS phase severely limits the possibility of detection.

As referred to in § 1, some information of dust-enshrouded protostars has been gleaned from the light re-emitted in the envelope. On the other hand, Morino et al. (1998) reported a unique indirect observation of an embedded massive protostar. They observed the infrared light from the Orion BN/KL nebula, which is scattered by dust grains far away from the exciting protostar. Direct light from the protostar is blocked by a torus-like structure on the line of sight toward us, but likely leaks in the polar direction and is scattered by the nebula. The color temperature of the scattered light is evaluated as $T_{\text{eff}} \simeq 3000 - 5500\text{K}$ from features of the absorption lines. The bolometric luminosity of the protostar is $L_{\text{bol}} > 4 \times 10^4 L_\odot$. If the scattered light is from the photosphere of the star, this low T_{eff} cannot be explained by a MS star: T_{eff} of a ZAMS star with the same luminosity is about 35000K , much higher than the above estimation. Morino et al. (1998) concluded that a very large stellar radius of $> 300 R_\odot$ is needed to explain the low effective temperature. Stimulated by this result, Nakano et al. (2000) studied the evolution of protostars with very high accretion rates $\sim 10^{-2} M_\odot/\text{yr}$ using a one-zone model. However, they concluded that stellar radius does not exceed $30 R_\odot$ and then failed to reproduce the observed low effective temperature. In contrast, using more detailed modeling, we have shown that the stellar radius in fact reaches as large as $\simeq 100 M_\odot$ in the cases of high accretion rate. In Figure 21, we present evolution of photospheric temperature and bolometric luminosity for three cases with $\dot{M}_* \geq 10^{-3} M_\odot/\text{yr}$. This figure shows that the required condition is satisfied, for example, with the case of $\dot{M}_* \geq 6 \times 10^{-3} M_\odot/\text{yr}$ for $M_* \simeq 20 - 25 M_\odot$. As a conclusion, the observation can be explained if the accretion rate is higher than $4 \times 10^{-3} M_\odot/\text{yr}$. The allowed mass range corresponds to the duration of the swelling of the protostar by the luminosity wave (see § 3.1). Recall that this swelling is caused by very inhomogeneous entropy distribution: the matter near the surface receives a large amount of entropy temporarily. Since this is not included in Nakano et al. (2000)'s one-zone model, their model gave a smaller radius than ours. In Appendix C, we present calibration of parameters for a polytropic one-zone model to include this effect approximately.

We have studied evolution of accreting protostars by solving the structure of the central growing stars and the surrounding accreting envelopes simultaneously. Particular attention is paid to cases with high accretion rates of $\dot{M}_* \geq 10^{-4} M_\odot/\text{yr}$, which are envisaged in some current scenarios of massive star formation. The protostellar evolution at a high mass accretion rate of $\dot{M}_* = 10^{-3} M_\odot/\text{yr}$ (run MD3 in Table 1) can be summarized as follows:

The entire evolution is divided into four characteristic phases; (I) adiabatic accretion ($M_* \lesssim 6 M_\odot$), (II) swelling ($6 M_\odot \lesssim M_* \lesssim 10 M_\odot$), (III) KH contraction ($10 M_\odot \lesssim M_* \lesssim 30 M_\odot$), and (IV) main-sequence accretion ($M_* \gtrsim 30 M_\odot$) phases.

A main driver of transition between the evolutionary phases above is a decrease in opacity in the stellar interior with increasing temperature, and thus protostellar mass. Due to the fast accretion, the matter accreted onto the stellar surface is embedded into the interior before radiatively losing the entropy produced at the accretion shock. Early in the evolution, the opacity in the stellar interior, which is mainly by free-free absorption, is very high owing to low temperature. As a result of the high opacity, the star keeps a large amount of entropy imported by the accreted matter. This is the adiabatic accretion phase (I). With the decrease in opacity, the entropy is transported outward gradually. When the matter near the surface temporarily has a large amount of entropy, the star expands as large as $\simeq 200 R_\odot$. This is the swelling phase (II). After that, all parts of the protostar lose energy and the protostar contracts. This is the KH contraction phase (III). With contraction, the temperature increases and the hydrogen burning eventually begins. When the nuclear burning provides sufficient energy to balance with that lost from the star radiatively, the star stops the KH contraction and reaches the zero-age main-sequence (ZAMS) phase at $\simeq 30 M_\odot$ (IV).

Deuterium burning plays little role in the evolution. Even if the deuterium burning is turned off by hand, the result hardly changes. The swelling (II) is caused by outward transfer of entropy within the star, which is observed as a propagating luminosity wave.

In general, at the higher accretion rate, the protostellar radius is larger and then the maximum temperature is lower at the same stellar mass, owing to the higher entropy within the protostar. As a result of the lower temperature, the onset of the nuclear burning is postponed to the higher protostellar mass.

For very high accretion rate $\dot{M}_* > 3 \times 10^{-3} M_\odot/\text{yr}$, in the course of the KH contraction, the radiation pressure onto the inner accreting envelope becomes so strong that the flow is retarded before hitting the stellar surface. The reduced ram pressure onto the stellar surface causes abrupt expansion of the star. The steady-state accretion is not possible thereafter. At this moment, the accretion might be halted, or might continue at a reduced rate or in a sporadic way. In either case, the evolution at the critical accretion rate of $M_{\text{cr}} = 3 \times 10^{-3} M_\odot/\text{yr}$ gives the upper mass limit of PMS stars at $\simeq 60 M_\odot$. Further growth of the star should be finally limited by the radiation pressure onto the outer dusty envelope. We have found this limit with M_{cr} gives the maximum mass of MS stars at $\simeq 250 M_\odot$.

Such a high accretion rate has also been expected and studied for the first star formation in the universe. The evolutions of primordial and solar-metallicity protostars are very similar at the same accretion rate. However, the lower opacity of the primordial gas results in the earlier transitions between the evolutionary phases above. For example, with $\dot{M}_* = 10^{-3} M_\odot/\text{yr}$, the accreting star enters the KH contraction phase at $10 M_\odot$ in the solar metallicity case, while it enters at $7 M_\odot$ in the primordial case.

Distinguishing features of those massive protostars accreting at high rates include the large stellar radius sometimes exceeding $100 R_\odot$, and then low color temperature $\simeq 6000\text{K}$. A massive protostar in Orion BN/KL nebula indeed has such features and is a possible candidate of such objects.

The authors thank Francesco Palla, Nanda Kumar, Jonathan Tan, Mark Krumholz, and Shu-ichiro Inutsuka for helpful comments and discussions. This study is supported in part by Research Fellowships of the Japan Society for the Promotion of Science for Young Scientists (TH) and by the Grants-in-Aid by the Ministry of Education, Science and Culture of Japan (18740117, 18026008, 19047004: KO).

REFERENCES

- Alexander, D.R. & Ferguson, J. W., 1994, ApJ, 437, 879
 Asplund, M., Grevesse, N. & Sauval, A.J., 2005, ASP Conf. Ser., 336, 25
 Beech, M. & Mitalas, R., 1994, ApJS, 95, 517
 Behrend, R. & Maeder, A., 2001, A&A, 373, 190
 Beltrán, M.T., Cesaroni, R., Codella, C., Testi, L., Furuya, R.S. & Olmi, L. 2006, Nature, 443, 427
 Beuther, H., Schilke, P., Sridharan, T.K., Menten, K.M., Walmsley, C.M. & Wyrowski, F. 2002, A&A, 383, 892
 Bernasconi, P.A. & Maeder, A. 1996, A&A, 307, 829
 Bonnell, I.A., Bate, M.R. & Zinnecker, H., 1998, MNRAS, 298, 93
 Clayton D., 1968, *Principles of Stellar Evolution and Nucleosynthesis*. McGraw-Hill, New York
 Cox, J.P. & Giuli, R.T., 1968, *Principles of Stellar Structure*, Gordon & Breach, New York
 Cunha, K., Hubeny, I. & Lanz, T. 2006, ApJ, 647, L143
 Ezer, D. & Cameron, A.G.W. 1971, Ap&SS, 14, 399
 Fazal, F.M., Sradharan, T.K., Qiu, K., Whitney, B., Robiraille, T. & Zhang, Q., 2007, astro-ph/0711.2261
 Figer, D.F., 2005, Nature, 434, 192
 Fuller, G.A., Williams, S.J. & Sridharan, T.K., A&A, 442, 949
 Grevesse, N. & Noels, A., 1993, Phys. Scr., T47, 133
 Hanson, M.M., Howarth, I.D. & Conti, P.S., 1997, ApJ, 489, 698
 Hayashi, C., Hoshi, R. & Sugimoto, D., 1962, Prog. Theor. Phys. Suppl., 22, 1
 Hopkins, A.M. & Beacom, J.F., 2006, ApJ, 651, 142
 Igrasias, C.A. & Rogers, F.J., 1996, ApJ, 464, 943
 Kahn, F.D., 1974, A&A, 37, 149
 Keto, E. & Wood, K., 2006, ApJ, 637, 850
 Krumholz, M.R. & Thompson, T.A., 2007, ApJ, 661, 1034
 Krumholz, M.R., Klein, R.I. & McKee, C.F., 2007, ApJ, 656, 959
 Kumar, M.S.N. & Grave, J.M.C., 2008, astro-ph/0802.2073
 Larson, R.B. & Starrfield, S. 1971, A&A, 13, 190
 Madau, P., Ferguson, H.C., Dickinson, M.E., Giavalisco, M., Steidel, C.C., Fruchter, A. MNRAS, 283, 1388
 Matsuda, T., Sato, H., & Takeda, H. 1969, Prog. Theor. Phys., 42, 219
 McKee, C.F. & Tan, J.C., 2002, Nature, 416, 59
 McKee, C.F. & Tan, J.C., 2003, ApJ, 585, 850
 McKee, C.F. & Ostriker, E.C., 2007, ARA&A, 45, 565
 Morino, J., Yamashita, T., Hasegawa, T. & Nakano, T., 1998, Nature, 393, 340
 Motte, F., Bontemps, S., Schilke, P., Schneider, N., Menten, K.M. & Brogiere, D., 2007, A&A, 476, 1243

- Nakano, T. 1989, *ApJ*, 345, 464
Nakano, T., Hasegawa, T., & Norman, C., 1995, *ApJ*, 450, 183
Nakano, T., Hasegawa, T., Morino, J. & Yamashita, T., 2000, *ApJ*, 534, 976
Norberg, P. & Maeder, A., 2000, *A&A*, 359, 1025
Omukai, K. & Nishi, R., 1998, *ApJ*, 508, 1410
Omukai, K. & Palla, F., 2001, *ApJ*, 561, 550L
Omukai, K. & Palla, F., 2003, *ApJ*, 589, 677
Osorio, M., Lizano, S. & D'Alessio, P., 1999, *ApJ*, 525, 808
Palla, F., Salpeter, E.E. & Stahler, S.W., 1983, *ApJ*, 271, 632
Palla, F. & Stahler, S.W., 1990, *ApJ*, 360, 47L
Palla, F. & Stahler, S.W., 1991, *ApJ*, 375, 288 (PS91)
Palla, F. & Stahler, S.W., 1992, *ApJ*, 392, 667
Palla, F. & Stahler, S. W., 1993, *ApJ*, 418, 414
Pollack, J.B., Hollenbach, D., Beckwith, S., Simonelli, D.P., Roush, T., Fong, W. 1994, 421, 615
Rathborne, J. M., Simon, R. & Jackson, J. M. 2007, *ApJ*, 662, 1082
Saslaw, W. C., & Zipoy, D. 1967, *Nature*, 216, 976
Schaller, G., Schaerer, D., Meynet, G. & Maeder, A., 1992, *A&AS*, 96, 269
Shu, F.H., Adams, F.C. & Lizano, S., 1987, *ARA&A*, 25 23
Stahler, S.W., 1983, *ApJ*, 274, 822
Stahler, S.W., 1988, *ApJ*, 332, 804
Stahler, S.W., Palla, F. & Salpeter, E.E., 1986, *ApJ*, 302, 590 (SPS86)
Stahler, S.W., Shu, F.H. & Taam, R.E., 1980, *ApJ*, 241, 637 (SST80a)
Stahler, S.W., Shu, F.H. & Taam, R.E., 1980, *ApJ*, 242, 226 (SST80b)
Stahler, S.W., Palla, F. & Ho, P.T.P., 2000, *Protostars and Planets IV*, 327
Tan, J.C. & McKee, C.F., 2004, *ApJ*, 603, 383
Weidner, C. & Kroupa, P., 2004, *MNRAS*, 348, 187
Wolfire, M.G. & Cassinelli, J.P., 1987, *ApJ*, 319, 850 (WC87)
Yorke, H.W. & Sonnhalter, C., 2002, *ApJ*, 569, 864
Yorke, H.W. & Bodenheimer, P., 2008, in *Astronomical Society of the Pacific Conference Series*, Vol. 387, ed. H.Beuther, H.Linz & T.Henning, p189
Yoshida, N., Omukai, K., Hernquist, L. & Abel, T., 2006, *ApJ*, 652, 6
Zhang, Q., Hunter, T.R., Brand, J., Sridharan, T.K., Cesaroni, R., Molinari, S., Wang, J. & Kramer, M., 2005, *ApJ*, 625, 864
Zinnecker, H. & Yorke, H.W., 2007, *ARA&A*, 45, 481

APPENDIX

A. METHOD OF CALCULATIONS

 A.1. *Evolutionary Calculations*

 A.1.1. *Protostar*

For protostellar structure, the following four stellar structure equations are solved:

$$\left(\frac{\partial r}{\partial M}\right)_t = \frac{1}{4\pi\rho r^2}, \quad (\text{A1})$$

$$\left(\frac{\partial P}{\partial M}\right)_t = -\frac{GM}{4\pi r^4}, \quad (\text{A2})$$

$$\left(\frac{\partial L}{\partial M}\right)_t = \epsilon - T \left(\frac{\partial s}{\partial t}\right)_M, \quad (\text{A3})$$

$$\left(\frac{\partial s}{\partial M}\right)_t = \frac{GM}{4\pi r^4} \left(\frac{\partial s}{\partial p}\right)_T \left(\frac{L}{L_s} - 1\right) C, \quad (\text{A4})$$

with a spatial variable of Lagrangian mass coordinate M . In the above, ϵ is the energy production rate by nuclear fusion, s is the entropy per unit mass, L_s is the radiative luminosity with adiabatic temperature gradient, and other quantities have ordinary meanings. The coefficient, C in equation (A4) is unity if $L < L_s$ (i.e., in radiative layers), and given by the mixing-length theory if $L > L_s$ (i.e., in convective layers). The momentum equation (A2) simply states the hydrostatic equilibrium. This is valid because the stellar mechanical timescale is generally much shorter than the accretion timescale. In energy equation (A3), on the other hand, the non-equilibrium term $-T(\partial s/\partial t)_M$ should be included. This is because the KH timescale can be longer than or comparable to the accretion timescale in our calculations. Thus, the thermal equilibrium is not generally satisfied in accreting protostars. Nuclear reactions included in ϵ are deuterium burning and hydrogen burning via the pp-chain and CN-cycle. The elements are homogeneously distributed in convective layers by the convective mixing.

There are two alternative schemes to integrate equations (A3) and (A4), which are the explicit and implicit schemes:

Explicit Scheme In the explicit scheme, equation (A3) is considered as a time development equation of the entropy. In order to update the entropy at each spatial grid from a time step $t - \Delta t$ to t , we use $(\partial L/\partial M)_t$ evaluated at the previous time step $t - \Delta t$ and calculate $(\partial s/\partial t)_M$ by equation (A3). Equation (A4) is transformed as,

$$L = L_s \left[1 + \frac{4\pi r^4}{GM} \left(\frac{\partial P}{\partial s}\right)_T \left(\frac{\partial s}{\partial M}\right)_t \right], \quad (\text{A5})$$

with $C = 1$ (radiative). We substitute the updated entropy gradient $(\partial s/\partial M)_t$ to equation (A5) and calculate the luminosity profile $L(M, t)$. This scheme enables the precise integration where the heat transport among mass cells is negligible, i.e., $(\partial L/\partial M)_t$ is much smaller than other terms in equation (A3). For example, this quasi-adiabatic situation is created in the very opaque interior of the protostar.

Implicit Scheme In the implicit scheme, on the other hand, time-derivative term $-T(\partial s/\partial t)_M$ in equation (A3) is regarded as a source term to calculate the luminosity profile by spatial integration. We simultaneously integrate equations (A3) and (A4), evaluating $(\partial s/\partial t)_M$ at every increment of spatial grids. This scheme works effectively where the heat transport among mass cells works to redistribute entropy. For example, this is the case near the stellar surface. Devote special attention to discretizing the time-derivative $(\partial s/\partial t)_M$ in equation (A3). For example, consider the gas element $\dot{M}_* \Delta t$ measured from the surface in a stellar model. This element accretes to the star from a time step $t - \Delta t$ to t , and is still in the accreting envelope at the previous time step $t - \Delta t$. The accreting matter plunges to the star through the accretion shock front, which is treated as a mathematical discontinuity in our formulation. Describing the derivative across the discontinuity is a problem. We avoid this difficulty adopting a coordinate conversion (SST80b),

$$\left(\frac{\partial s}{\partial t}\right)_M = \left(\frac{\partial s}{\partial t}\right)_m + \dot{M}_* \left(\frac{\partial s}{\partial m}\right)_t, \quad (\text{A6})$$

where m is the inverse mass coordinate $m \equiv M_* - M$. The term $(\partial s/\partial t)_m$ can be obtained only with the entropy distribution within the shock front. This treatment is fairly valid, because the structure of the settling layer hardly changes over a few time steps, observing from the shock front.

In our calculations, we properly adopt different schemes in different evolutionary stages. In the early phase of the evolution, we use both the explicit and implicit schemes to construct one stellar model (e.g., SST80b); the explicit scheme is used in the deep interior and is switched to the implicit scheme near the stellar surface. First, we solve the interior with the explicit scheme; we integrate equations (A1) and (A2) outward with a guess of central pressure P_c . When the explicitly solved region is radiative, we calculate $L(M, t)$ with equation (A3). Once active deuterium burning begins, however, the explicit update of entropy sometimes makes negative entropy gradients $(\partial s/\partial M)_t < 0$. Such a layer should be regarded

as a convective layer, and equation (A5) is not valid any more. We temporarily change the integration method in such a layer. We correct the entropy distribution as $(\partial s/\partial M)_t = 0$ there after the explicit update, following the “equal-area rule” developed by SST80b. Once the entropy profile is corrected, we calculate $(\partial s/\partial t)_M$ and obtain the luminosity distribution by integrating equation (A3). As the integration approaches the surface, the term $(\partial L/\partial M)_t$ in equation (A3) gradually grows. We switch to the implicit method where $(\partial L/\partial M)_t$ attains $0.5\dot{M}_*T(\partial s/\partial m)_t$. We integrate all equations (A1) – (A4) with a guess of the entropy at the switching point s_{sw} . When the integration reaches the stellar surface, we check the differences from the required boundary conditions (see § A.1.2 below). We improve the guessed values of P_c and s_{sw} , and iterate this procedure until the model satisfies the outer boundary conditions.

The above method successfully works in the early phase of evolution. However, only in the later stage of evolution, where the entropy redistribution among mass cells works even in the deep stellar interior, we need to use another method with the implicit scheme. This occurs when a widespread convective layer appears during active deuterium burning, or when radiative heat transport becomes efficient due to the opacity decrease in the deep interior (see § 3 for detail). In the fully implicit method, we integrate the equations (A1) – (A4) outward from the center with a guess of the central pressure P_c and entropy s_c . If the integration reaches the stellar surface, we advance to the same fitting process at the surface as in the above method. If the integration diverges and fails before reaching the surface, we adopt another shooting method to a halfway fitting point. We additionally guess the radius R_* and luminosity L_* at the stellar surface, and integrate backward to the fitting point. We adjust boundary values to match the physical quantities at the fitting point, which are obtained by the forward and backward integrations.

A.1.2. Accreting Gas Envelope and Accretion Shock Front

The outer boundary condition of the protostar is given by constructing the structure of an accreting gas envelope. The boundary layer connecting the accreting envelope and protostar actually has detailed structure. The accreted gas initially hits a standing shock front and is heated up by compression there. The shocked gas next enters the relaxation layer behind the shock front and is cooled down by radiative loss. In our formulation, this detailed structure is not solved, but treated as a mathematical discontinuity (SST80). We define the following two points across the discontinuity: a post-shock point, where gas and radiation temperature first become equal behind the relaxation layer, and a post-shock point ahead of the shock front. In our calculations, the former is the outer boundary of the protostar, and the latter is the inner boundary of the accreting envelope. Physical states at each point are related by a radiative shock jump condition.

Here, we focus on cases where the post-shock quantities are given in advance by the trial outward integration of the protostar (see § A.1.1). When the outward integration fails and the shooting to a halfway fitting point is needed, we only slightly modify the same procedure (e.g., see PS91). First, we judge if the accreting envelope is optically thin or thick. Temporarily assuming that the accretion flow is optically thin and in the free-fall, velocity and mass density at the pre-shock point are,

$$u_{\text{pre}} = -\sqrt{\frac{2GM_*}{R_*}}, \quad (\text{A7})$$

$$\rho_{\text{pre}} = \frac{\dot{M}_*}{4\pi R_*^2 u_{\text{pre}}}. \quad (\text{A8})$$

Ahead of the shock front, outward radiation comes from both the stellar interior and relaxation layer behind the shock front. Therefore, radiation temperature at the pre-shock point is written as,

$$T_{\text{rad,pre}} = \left(\frac{L_* + L_{\text{acc}}}{4\pi R_*^2 \sigma} \right)^{1/4}, \quad (\text{A9})$$

where σ is the Stefan-Boltzmann constant, and L_{acc} is the accretion luminosity defined by equation (3). Using equations (A7) – (A9), optical thickness of the accreting envelope is estimated as,

$$\tau_{\text{pre}} = R_* \rho_{\text{pre}} \kappa(\rho_{\text{pre}}, T_{\text{pre}}), \quad (\text{A10})$$

where κ is the Rosseland mean opacity. If $\tau_{\text{pre}} < 1$, the accreting envelope is optically thin and initial adoption of the thin envelope is verified. The jump condition at the accretion shock front is provided by considering the flow structure across the shock front (SST80b). In the optically-thin case, the post-shock temperature is related to the stellar radius and luminosity (PS91),

$$T_{\text{post}} = \left[\frac{1}{4\pi R_*^2 \sigma} \left(\frac{1}{2}L_* + \frac{3}{4}L_{\text{acc}} \right) \right]^{1/4}. \quad (\text{A11})$$

This is the outer boundary condition of the protostar. The protostellar models are constructed for the post-shock quantities to satisfy equation (A11).

If $\tau_{\text{pre}} > 1$, on the other hand, the accreting envelope should actually be optically thick. In this case, we solve structure of the flow inside the photosphere, i.e., radiative precursor. First, we determine the locus of the photosphere. Assuming the free-fall flow outside the photosphere, optical depth to the photosphere τ_{ph} can be written following equations (A7) – (A10) by substituting physical quantities at the photosphere. The only unknown quantity is the luminosity at the

photosphere L_{ph} , which is needed to calculate temperature in equations (A9). We calculate this photospheric luminosity using the conservation law of the net energy outflow rate L_e through the precursor,

$$L_e = L_{\text{ph}} - \dot{M}_* \left(h_{\text{ph}} + \frac{1}{2} u_{\text{ph}}^2 - \frac{GM_*}{R_{\text{ph}}} \right), \quad (\text{A12})$$

where $h_{\text{ph}} = h(\rho_{\text{ph}}, T_{\text{ph}})$ is the enthalpy of both gas and radiation at the photosphere. Using the known post-shock quantities, we can give the numerical value of L_e at the bottom of the accretion flow,

$$L_e = L_* - \dot{M}_* \left(h_{\text{post}} + \frac{1}{2} u_{\text{pre}}^2 - \frac{GM_*}{R_*} \right). \quad (\text{A13})$$

Assigning this value to L_e in equation (A12), the photospheric luminosity is written with the infall velocity and thermal state at $r = R_{\text{ph}}$. Consequently, T_{ph} and τ_{ph} are given as implicit functions of R_{ph} . Therefore, we can fix R_{ph} in an iterative fashion by requiring $\tau_{\text{ph}} = 1$. Once the photospheric radius is fixed, we solve the structure of the precursor by integrating the following equations inward from the photosphere,

$$\rho = -\frac{\dot{M}_*}{4\pi r^2 u}, \quad (\text{A14})$$

$$u \frac{\partial u}{\partial r} = -\frac{GM_*}{r^2} - \frac{1}{\rho} \frac{\partial P}{\partial r} + \frac{\kappa}{c} F, \quad (\text{A15})$$

$$\frac{\partial T}{\partial r} = -\frac{3\rho\kappa}{16\sigma T^3} F, \quad (\text{A16})$$

where F is the radiative flux. Using equations (A12) and (A14), F is written as a function of ρ , u , and T ,

$$F = -\rho u \left(\frac{L_e}{\dot{M}_*} + h + \frac{1}{2} u^2 - \frac{GM_*}{r} \right). \quad (\text{A17})$$

When the integration reaches the pre-shock point, a jump condition bridges the the pre-shock and post-shock points. An isothermal jump condition is applied for the optically-thick radiative shock front,

$$T_{\text{post}} = T_{\text{pre}}. \quad (\text{A18})$$

This is another outer boundary condition in addition to equation (A11).

A.2. Initial Models

We construct initial models by solving their structure. The method of calculation is based on that of evolutionary calculations, but with slight modifications. First, we assume the entropy distribution in the stellar interior as an increasing function with M ,

$$s(M) = s_{c,0} + \beta \frac{k_{\text{B}}}{m_{\text{H}}} \frac{M}{M_{*,0}}, \quad (\text{A19})$$

where $s_{c,0}$ is specific entropy at the stellar center, k_{B} is Boltzmann constant, m_{H} is atomic mass unit, and β (> 0) is a free parameter. In the core interior, we integrate equations (A1) and (A2) outward beginning with guessed $s_{c,0}$ and central pressure, p_c . According to equation (A5), the luminosity profile there is calculated using an entropy gradient obtained from (A19). Whereas this procedure is valid in the adiabatic interior, entropy and luminosity profiles should be consistently calculated in place of equation (A19) near the surface (also see § A.1.1). The switching point is defined as follows. Using equations (A3) and (A6), the energy equation can be written as,

$$\left(\frac{\partial L}{\partial M} \right)_t = \dot{M}_* T \left(\frac{\partial s}{\partial M} \right)_t, \quad (\text{A20})$$

omitting the nuclear energy production and time-derivative terms. Once the luminosity gradient $(\partial L/\partial M)_t$ becomes comparable to $\dot{M}_* T (\partial s/\partial M)_t$ calculated with equation (A19), we solve the full equations including equation (A20). The guessed $s_{c,0}$ and p_c are adjusted so that the core satisfies outer boundary conditions, as explained in § A.1.2. We have confirmed that some variations of initial models only affect subsequent protostellar evolution in a very early phase. In this paper, we adopt $\beta = 1$ as the entropy slope in equation (A19).

A.3. Opacity Tables

For the opacity, we adopt OPAL tables (e.g., Iglesias & Rogers 1996) with the composition given by Grevesse & Noels (1993) for temperature $T > 7000$ K. For $T < 7000$ K, we use other opacity tables based on calculations by Alexander & Ferguson (1994). Contribution from grains is excluded in the adopted composition (Asplund, Grevesse & Sauval 2005; Cunha, Hubeny & Laney 2006). In all runs, we adopt $X = 0.7$, $Y = 1 - X - Z$, and relative abundances of heavy elements following Grevesse & Noels (1993) composition.

B. COMPARISON WITH PREVIOUS WORK
 – EVOLUTION WITH THE LOW ACCRETION RATE OF $10^{-5} m_{\odot}/\text{yr}$ –

In § 3.2, we have presented the calculated protostellar evolution at the low accretion rate of $10^{-5} M_{\odot}/\text{yr}$ (run MD5). Whereas our numerical results reproduce basic features obtained by previous work (e.g., SST80a, PS91), there are still some differences. In this appendix, we examine causes of these differences by exploring some cases with different deuterium abundances and initial models.

B.1. *Dependence on Deuterium Abundance*

The effect of different deuterium abundances on the stellar interior structure in early phases is shown in Figure B22 for cases with $[D/H] = 3 \times 10^{-5}$, 2.5×10^{-5} , and 1×10^{-5} . The middle panel is the same as Figure 7 (upper), but reproduced for comparison. As described in § 3.2, our run MD5 exhibits somewhat complex evolution of convective layers in the early phase. A convective layer first appears at $M_* \simeq 0.3 M_{\odot}$, just after the deuterium burning begins. This convective layer disappears at $M_* \simeq 0.6 M_{\odot}$. The second convective layer emerges just outside the former outer boundary of the first one at $M_* \simeq 0.7 M_{\odot}$, and quickly reaches the surface. SST80a calculated the same model, but did not observe such a complex evolution. In their calculation, the first convective layer survives and eventually incorporates most of the stellar interior.

This difference comes from the fact that the evolution of convective layers sensitively depends on the initial deuterium abundance. For example, in the case with the deuterium abundance $[D/H] = 3 \times 10^{-5}$ (Figure B22 upper; run MD5-dh3), slightly higher than the fiducial value, the convective layer first appears at the same epoch as the fiducial case with $[D/H] = 2.5 \times 10^{-5}$, and extends outward. In this case, another convective layer soon emerges at the surface and begins to extend inward. These two convective layers finally merge at $M_* \simeq 0.6 M_{\odot}$, and render most of the interior convective. At $M_* \simeq 1 M_{\odot}$, the convective region contains about 97% of the total mass. These features are very similar to those found by SST80a, who terminated their calculation at $M_* = 1 M_{\odot}$. Our calculation shows that the subsequent evolution in this case is almost the same as in our fiducial run MD5. The central radiative core gradually expands as the stellar mass increases, and finally occupies most of the interior at $M_* \simeq 4 M_{\odot}$.

This sensitive dependence on the deuterium abundance is explained as follows. The expansion of convective layers is caused by increase of the specific entropy within it, which is generated by the nuclear burning at the bottom of the layer. For continuing expansion of the convective layer, deuterium needs to be supplied continuously. Fresh deuterium becomes available when the convective layer newly incorporates the radiative region. This deuterium immediately spreads over the convective layer, and is consumed for further nuclear fusion. For sufficiently high deuterium abundance, acquired deuterium is high enough to maintain the active nuclear burning. In this case, the convective layer continuously grows as in the case with $[D/H] = 3 \times 10^{-5}$ (run MD5-dh3). On the other hand, for low deuterium abundances, the nuclear burning becomes too weak to maintain development of the convective layer. The convective layer ceases to grow and disappears as in the case with $[D/H] = 2.5 \times 10^{-5}$ (run MD5). For even smaller deuterium abundance $[D/H] = 1 \times 10^{-5}$ (Fig. B22, lower; run MD5-dh1), no convective layer appears even after ignition of the deuterium burning until at $M_* \sim 0.8 M_{\odot}$, when the surface convective layer finally emerges. In this case, the subsequent mass-radius relation is almost same as in the case without deuterium burning (run MD5-noD) although the surface convective layer persists until $M_* \sim 3 M_{\odot}$. Our fiducial run MD5 is just intermediate between the deuterium-rich (run MD5-dh3) and -poor (MD5-dh1) cases presented in Figure B22. Therefore, a slight difference in input physics affects the internal structure significantly.

B.2. *Effect of Difference in Initial Models*

Evolution of accreting intermediate-mass ($1 M_{\odot} < M_* < 8 M_{\odot}$) protostars have been studied in some previous work (e.g., PS91). Our results agree well with the previous work, but still show some differences even with the same accretion rate, which can be ascribed to different initial models. Whereas our initial model is a tiny radiative protostar with $\ll 1 M_{\odot}$ (see § A.2), the initial model of PS91, for example, is a $1 M_{\odot}$ fully-convective protostar. We confirmed that our code reproduces almost the same evolution as that of PS91, if we begin the calculation with the same initial model.

The initial model of PS91 is constructed in a manner similar to that described in § A.2. The homogeneous entropy distribution is adopted in place of equation (A19), and its value is taken from the semi-analytic model of Stahler (1988). We have reconstructed the model of Stahler (1988), and obtained $s_{c,0} = -4.12 k_B/m_H$ for a $1 M_{\odot}$ star with our adopted opacity tables. As in § A.2, we separately solve the core interior and the surface super-adiabatic layer. First, we integrate the core interior outward from the center with a guessed value of the central pressure. We also guess the luminosity at the bottom of the surface super-adiabatic layer in advance, and record the entropy gradient $\partial s/\partial M$ using equation (A4). Once the recorded $\partial s/\partial M$ attains a small finite value, we switch the scheme and integrate all equations (A1) – (A4). The guessed quantities are adjusted for the core to satisfy the outer boundary conditions. The constructed model is a fully convective star, whose mass and radius are $1 M_{\odot}$ and $4.2 R_{\odot}$.

We calculate the subsequent evolution beginning with this initial model (run MD5-ps91). Figure B23 shows the evolution of such a protostar. Our calculation reproduces the basic features of a calculation done by PS91, which adopted the same accretion rate and accretion-shock outer boundary. In an early phase, the star remains fully convective and deuterium burning occurs around the stellar center. Deuterium concentration significantly falls in this phase. This is because the central temperature continuously increases, and total burning rate L_D slightly exceeds the steady burning rate $L_{D,st}$ (e.g., Palla & Stahler 1993). These features are somewhat different from our fiducial run MD5, where a radiative core persists throughout the evolution and gradually expands with the increase in M_* by accretion (see Fig. 7). These differences come from different initial models. Figure 7 also shows that mass-averaged deuterium concentration $f_{d,av}$ does not fall

much below 0.01 in our run MD5. This is because the deuterium burning layer gradually moves to the outer layer, where temperature is always around 10^6 K and $L_D \sim L_{D,st}$. At $M_* = 2 M_\odot$, for example, $f_{d,av} \sim 0.04$ in run MD5, but only $f_{d,av} \sim 10^{-5}$ in run MD5-ps91. Therefore, our calculation predicts that intermediate-mass protostars have a larger amount of deuterium than assumed by PS91. Figure B23 shows that the fully convective phase ends at $M_* \simeq 2.6 M_\odot$, when a thin radiative layer, i.e., radiative barrier, suddenly appears within the star. The radiative barrier blocks inward convective transport of the accreted deuterium. Consequently, the inner region, where deuterium has run out, immediately returns to being radiative. After that, the convective layer remains only above the radiative core, and deuterium burning occurs at the bottom of the convective layer. As in our fiducial run MD5, the protostar swells up at $M_* \simeq 3.4 M_\odot$. PS91 have

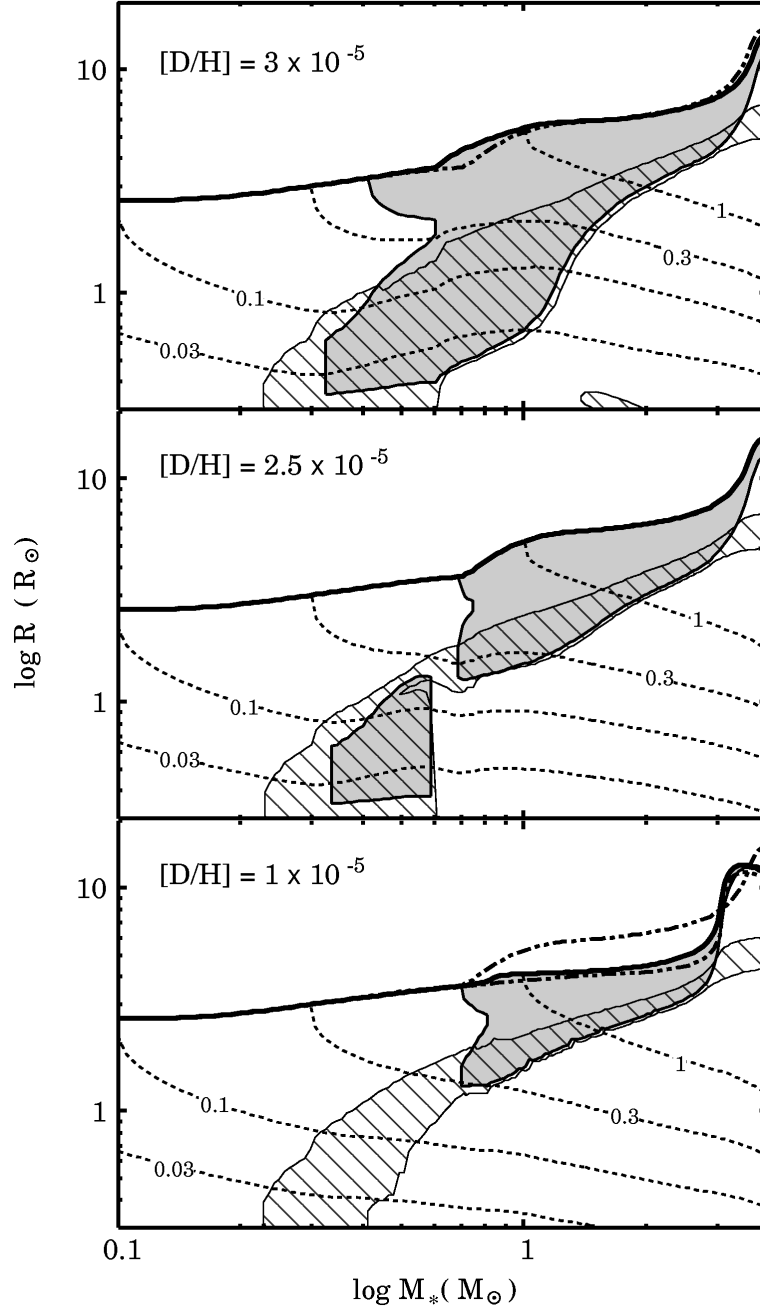


FIG. B22.— The interior evolution in early phases for different deuterium abundances with the accretion rate $\dot{M}_* = 10^{-5} M_\odot/\text{yr}$. The deuterium abundances are $[D/H] = 3 \times 10^{-5}$ (top; run MD5-dh3), 2.5×10^{-5} (middle; MD5), and 1×10^{-5} (bottom; MD5-dh1). Properties of the interior structure are presented in the same manner as in Fig. 2. In each panel, the thick solid line represents the position of the accretion shock front. The convective regions are shown by the gray-shaded area. In the top (bottom) panel, the position of the accretion shock front for $[D/H] = 2.5 \times 10^{-5}$ ($[D/H]=0$, run MD5-noD) is plotted with the dot-dashed curve for comparison.

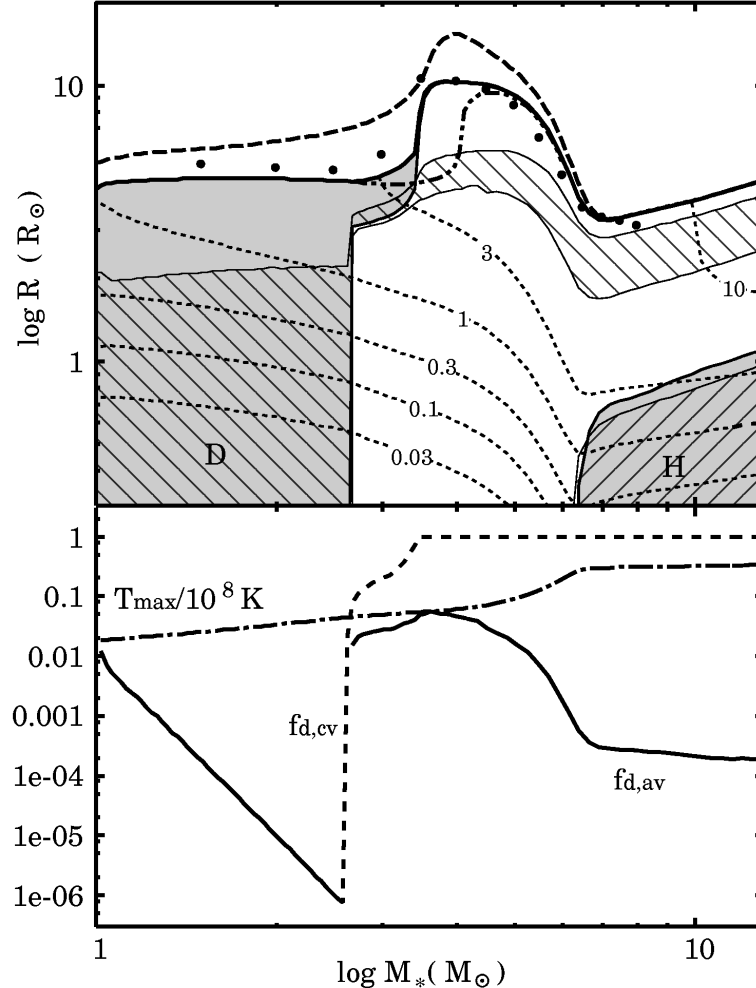


FIG. B23.— Same as Fig. 7 but for the different initial model calculated following PS91 (run MD5-ps91). In the upper panel, the filled circles denote the protostellar radius by PS91 with the same parameter as our fiducial case (MD5), which is shown by the dashed curve. PS91 started calculation at $M_{*,0} = 1 M_{\odot}$, while the initial mass in our calculation is much smaller $M_{*,0} = 0.01 M_{\odot}$. The dot-dashed curve also presents the protostellar radius in run MD5-ps91, where the deuterium burning is turned off at $M_* = 2.7 M_{\odot}$, when a radiative barrier emerges within the star (see text).

concluded that this swelling is caused by the shell-burning of deuterium. To see the role of the deuterium shell-burning in the swelling, we also calculate evolution with cessation of the deuterium burning after the appearance of the radiative barrier. We find that the swelling occurs similarly, although it is slightly delayed, even without deuterium burning. This is caused by the outward transport of embedded entropy, which is observed as propagation of a luminosity wave (see § 3.1 and 3.2). Although PS91 have attributed the swelling only to the shell-burning of deuterium, we conclude that the main driver of the swelling is always the propagation of the luminosity wave. After the turn-around of the radius, the star enters the subsequent KH contraction phase. The calculated mass-radius relation thereafter gradually converges with that in our fiducial run MD5. The epoch of the Hydrogen burning, $M_* \simeq 7 M_{\odot}$, also agrees with that in the fiducial run.

C. CALIBRATION OF ONE-ZONE MODEL

While detailed numerical calculations as in this paper are a direct method to study the structure of accreting protostars, one-zone modeling with the polytropic equation of state $P = K\rho^{1+1/N}$ is also a useful way. In the one-zone models of protostellar evolution, which were originally developed by Nakano, Hasegawa, & Norman (1995), an energy budget of the protostar is considered. The total energy of the star E and its time-derivative dE/dt are written as functions of the stellar mass M_* and radius R_* respectively. The mass-radius relation is obtained by substituting the equation E into dE/dt . Nakano et al. (2000) applied such a model to study protostellar evolution at the very high accretion rate of $\dot{M}_* \sim 10^{-2} M_{\odot}/\text{yr}$. McKee & Tan (2003) improved the model by calibrating it with numerical calculations at the accretion rates of $\leq 10^{-4} M_{\odot}/\text{yr}$ (e.g., PS91). Tan & McKee (2004) also showed that the one-zone models can reproduce the mass-radius relations of primordial protostars at the high accretion rates $\sim 10^{-3} M_{\odot}/\text{yr}$ (e.g., Omukai & Palla 2003).

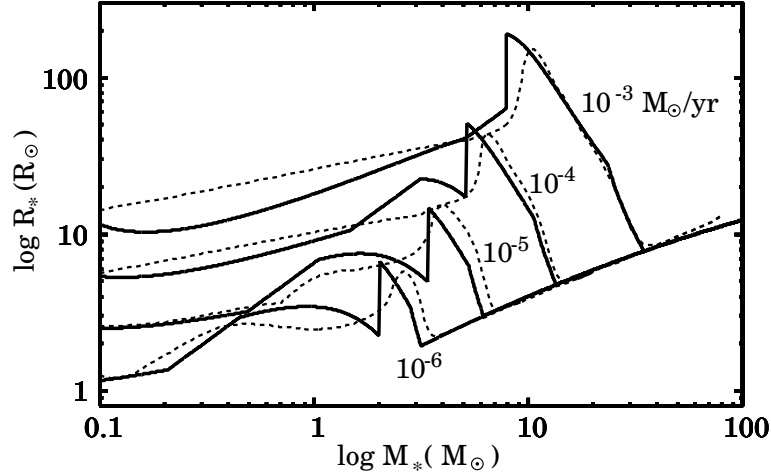


FIG. C24.— Comparison between the protostellar radii calculated by the one-zone models based on McKee & Tan (2003) but with parameters calibrated as in Sec.C (solid) and by our numerical models (dotted). The cases with the accretion rates from 10^{-6} to $10^{-3} M_{\odot}/\text{yr}$ are shown.

Here, we present one-zone models reproducing our numerical results (Fig. C24). These models are constructed following McKee & Tan (2003) with some improvements. Our numerical calculations have shown that protostars are initially radiative for any accretion rate. With an accretion rate less than $10^{-4} M_{\odot}/\text{yr}$, the convective layers gradually extend as deuterium burning becomes significant. Since the polytropic models with index $N = 1.5$ and $N = 3$ approximate a fully convective and radiative star respectively (e.g., Cox & Giuli 1968), we adopt intermediate values: $N = 2.5$ for $\dot{M}_* \leq 10^{-5} M_{\odot}/\text{yr}$ and slightly larger values for higher accretion rates, $N = 2.5 + 0.25 \log(\dot{M}_*/10^{-5} M_{\odot}/\text{yr})$. Initial masses and radii are arbitrarily taken as $M_{*,0} = 0.1 M_{\odot}$ and $R_{*,0} = 2.5 R_{\odot} (\dot{M}_*/10^{-5} M_{\odot}/\text{yr})^{1/3}$. The steady deuterium burning is assumed to begin when the central temperature reaches 1.5×10^6 K. After that, we adopt $N = 1.75$, which is slightly larger than the fully convective value $N = 1.5$, to resemble our numerical result, where a radiative core gradually expands with the increase of the stellar mass (see § 3.2). Subsequently, the protostar swells up with the propagation of the luminosity wave. We include this effect into the model by artificially increasing the stellar radius by a factor of 3 to fit the calculated mass-radius relations. We assume that this occurs when the ratio $t_{\text{KH}}/t_{\text{acc}}$ reaches 1.75. Other adjustments of models are the same as those of McKee & Tan (2003). The presented one-zone models fit our mass-radius relations within 30% deviation except in very early phases for high accretion rates.